Master's thesis

NTNU
Norwegian University of Science and Technology
Faculty of Natural Sciences
Department of Physics

Magnus Kristoffersen

Phase-Field Modelling of Precipitation Mechanisms in Al-Mg-Si Alloys

Master's thesis in Physics
Supervisor: Jaakko Akola
May 2022

NTNU
Norwegian University of
Science and Technology

Magnus Kristoffersen

Phase-Field Modelling of Precipitation Mechanisms in Al-Mg-Si Alloys

Master's thesis in Physics
Supervisor: Jaakko Akola
May 2022

Norwegian University of Science and Technology
Faculty of Natural Sciences
Department of Physics

NTNU
Norwegian University of
Science and Technology

Abstract

In this master's thesis, the precipitation process of β'' precipitates during artificial ageing of 6xxx-series aluminium alloys is studied using the phase-field method. During the last two decades, experimental studies have been conducted with an external field across a sample of aluminium alloy during artificial ageing. These studies found that the application of an external field resulted in higher peak hardness values and shorter ageing time compared to the conventional artificial ageing process. The work in this thesis considers the effect of the electron wind on the microstructure, caused by applying a direct electric current across the sample. The elastic strain contributions due to the misfit between the aluminium host matrix and the precipitate phase is also implemented into the phase-field model to obtain the correct needle-like shape of the precipitates.

The calculation of a characteristic time scale for the diffusion of temperature in the microstructure is performed, finding that a temperature front propagates 100 nm in the course of $t = 156\,\mathrm{ps}$, indicating that temperature fluctuations can be neglected in microstructure modelling. The simulation results connected to the applied direct current does not attain the same evolution mechanisms as those presented in experimental studies of similar systems, which may indicate that the contribution from the electron wind in real alloys is small compared to other evolution mechanisms.

Sammendrag

Denne masteravhandlingen studerer utfellingsprosessen av β'' utfellinger under kunstig eldning av aluminiumslegeringer i 6xxx-serien ved å benytte seg av fase-felt metoden. I løpet av de siste to tiårene har det blitt utført eksperimentelle studier der et eksternt felt ble satt på over en legeringsprøve av en aluminiumslegering samtidig som prøven var under kunstig eldning. Disse studiene oppdaget at legeringsprøvene oppnådde høyere maksimal styrke og raskere eldning under denne behandlingen. Arbeidet i denne avhandlingen ser på effekten av elektronvind på mikrostrukturen, forårsaket av at det blir satt på en elektrisk likestrøm gjennom legeringsprøven. Bidraget fra elastisk tøyning som følge av at gitterstrukturen til β'' utfellingene passer dårlig inn i aluminiumsgitteret blir også lagt til i fase-felt modellen for å oppnå den typiske nål-formen til disse utfellingene.

Det blir beregnet en karakteristisk tidsskala for diffusjonen av temperatur i mikrostrukturen som kommer frem til at det tar $t = 156\,\mathrm{ps}$ å propagere en temperaturfront 100 nm, og dette indikerer at temperatursvingninger kan ses bort fra i modellering av mikrostrukturen. Simuleringsresultatene tilknyttet systemet med påført elektriske likestrøm over legeringsprøven oppnår ikke de samme utviklingsmekanismene i mikrostrukturen som har blitt sett i eksperimentelle undersøkelser av lignende systemer. Dette kan indikere at bidraget fra elektronvinden utgjør lite i forhold til andre utviklingsmekanismer i legeringer.

Acknowledgements

I want to express my deepest gratitude to Dr. David Kleiven for his support and guidance throughout this past year. I am grateful for all the advice, insight and relevant literature you shared with me, and especially for being available for discussions and advice after finishing your time at NTNU. I also want to sincerely thank my supervisor, Prof. Jaakko Akola, for productive discussions and feedback.

I would like to thank my friends Martin, Javid and Sepehr for all the unforgettable memories we have made during our time in Trondheim. Finally, I would like to thank my parents for their constant support throughout everything I do, for believing in me, and for always encouraging me to work hard towards my goals.

Contents

List of Figures

Abbreviations

CALPHAD CALculation of PHAse Diagrams.

DC direct current.

DFT density functional theory.

FCC face-centred cubic.

FEM finite element method.

GP zones Guinier-Preston zones.

INL Idaho National Laboratory.

MOOSE Multiphysics Object-Oriented Simulation Environment.

PDEs partial differential equations.

PJFNK Preconditioned Jacobian Free Newton Krylov.

SSSS supersaturated solid solution.

TEM transmission electron microscopy.

Chapter 1

Introduction

The properties of aluminium alloys depend on the combinations and concentrations of alloying elements, making it possible to choose an alloy depending on the properties needed for a product. This makes aluminium one of the most versatile metallic materials and is consequently used in a variety of industries, such as the automotive and the aircraft industry [1–4]. Some of the beneficial properties of aluminium alloys for these industries are high corrosion resistance, lightweight, high strength to weight ratio and that they are easily formed by extrusion or casting. Many of the alloys are hardened through a heat treatment process to achieve the high strength to weight ratio, and these are denoted as heat-treatable alloys. The increase in strength through this process is caused by the formation of precipitates in the atomic structure, which are structures with high concentrations of the alloying elements and lattice mismatch with the Al host matrix. The non-heat-treatable alloys are instead hardened by work hardening. Wrought aluminium alloys are classified by a four-digit number system, where the first digit indicates the principal alloying elements of the alloy. The alloys in the 2xxx-, 6xxx-, 7xxx- and some of the alloys in the 8xxx-series are heat-treatable, while the remaining alloys are non-heat-treatable [1, 5]. The main applications of the different aluminium alloy series are shown in Fig. 1.1.

During the last two decades, experimental studies have been conducted with an external field applied across an alloy sample during the aging process [7–10]. These experiments were carried out to study how the evolution of the material

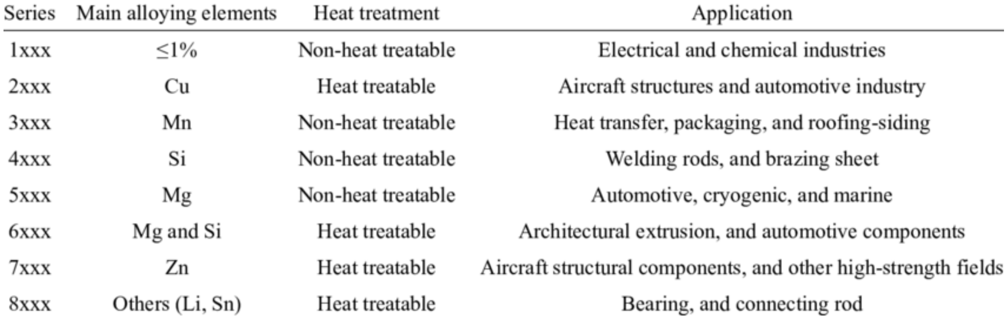

Series	Main alloying elements	Heat treatment	Application
1xxx	≤1%	Non-heat treatable	Electrical and chemical industries
2xxx	Cu	Heat treatable	Aircraft structures and automotive industry
3xxx	Mn	Non-heat treatable	Heat transfer, packaging, and roofing-siding
4xxx	Si	Non-heat treatable	Welding rods, and brazing sheet
5xxx	Mg	Non-heat treatable	Automotive, cryogenic, and marine
6xxx	Mg and Si	Heat treatable	Architectural extrusion, and automotive components
7xxx	Zn	Heat treatable	Aircraft structural components, and other high-strength fields
8xxx	Others (Li, Sn)	Heat treatable	Bearing, and connecting rod

Figure 1.1. *Overview of the main applications of the different series of aluminium alloys. Reprinted from Wang et al. [6].*

properties is affected by applying an external field during ageing. Zhang et al. [9] applied a low density electric pulse current during the ageing of 2219 aluminium alloy to compare the hardness evolution against conventional ageing experiments. They found that the necessary ageing time to reach the peak hardness value was shorter than for conventional experiments, as seen in Fig. 1.2. He et al. [7] applied a direct current during ageing of a 7B04 aluminium alloy sample, and found that the peak conductivity, tensile strength and elongation were higher for the sample aged with applied direct current. While these effects have been studied through experimental work, there have been a lack of computer simulations to study the precipitation mechanisms caused by the applied field. In this thesis, we simulate the microstructural evolution with and without an applied external field in aluminium alloys of the 6xxx-series in order to study and compare the precipitation mechanisms. These alloys have magnesium and silicon as their principal alloying elements and are often denoted as Al−Mg−Si alloys. We choose to study this alloy series because the majority of extruded aluminium products in Western Europe consists of these alloys [11].

The main focus of this thesis is to study the precipitation mechanisms of β'' precipitates in Al−Mg−Si alloys during artificial ageing through computer simulations. There is also made an effort to model the effects of applying a DC electric field across an alloy sample in the ageing process. The simulations are modelled using the phase-field method, as this method has been found to be versatile and efficient for modelling microstructure evolution with nucleation processes [12–14].

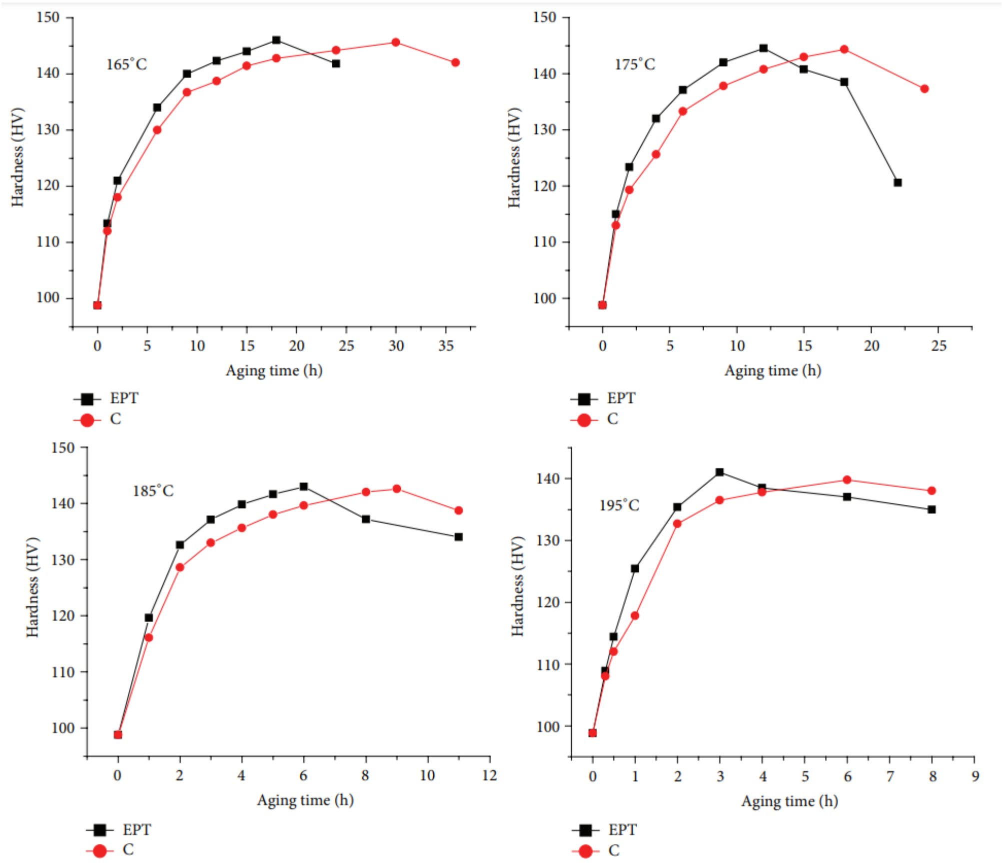

Figure 1.2. *Reprinted hardness plots from the experimental work by Zhang et al. [9]. The graphs denoted by EPT refers to alloy samples that were artificially aged with an applied pulse current across the sample, where the maximum current was* $I_{\max} \approx 20\,\mathrm{A}$. *The graphs denoted by C refers to the samples that were aged without an applied current.*

The main applications of the phase-field method are modelling solidification, solid-state phase transformations and grain growth systems [15]. This method describes a system using conserved and non-conserved field variables and it models the interface between phases using a diffuse-interface approach, making it unnecessary to trace the phase boundaries like in sharp-interface systems. Additionally, the contributions from other fields, such as elastic and electric fields, can be implemented into phase-field models in a straightforward manner. The phase-field calculations in this thesis are performed using the Multiphysics Object-Oriented Simulation Environment (MOOSE) framework, which is an open-source, parallel finite element framework [16]. The model parameters and simulation inputs are reported in detail, and an input file for solving the phase-field model with contributions from an applied DC field is appended as supplementary material in Section A, to make the simulations in this work reproducible and easily extended in future work.

The thesis begins by introducing the heat treatment and precipitation process of Al−Mg−Si alloys. Then, the theory of the phase-field method and the additional terms and equations related to the contributions from elastic strain and a DC electric field are derived. The choice of a free energy density expression and the parameter values used in the model are also motivated. The next chapter goes through the implementation of the phase-field model into the MOOSE framework, starting with a general introduction to the framework. Since this framework uses the finite element method (FEM) to solve partial differential equations, this method is presented and then applied to the phase-field equations. The MOOSE framework contains a probabilistic nucleation model, which is also implemented in the simulations.

The results and discussion chapter starts by looking at the effect of allowing temperature fluctuations in the simulation, where a characteristic time scale for the diffusion of temperature is calculated. Through this work, we find that it is unnecessary to account for temperature fluctuations in the microstructure because the high thermal diffusivity of aluminium alloys leads to a characteristic time scale of 156 ps for a temperature front to propagate a distance of 100 nm. Then, the results of simulations with different contributing fields are presented, where the fraction of precipitated area and the shapes and sizes of the precipitates in the simulations are compared and discussed. When simulating the effects of the applied DC electric field across the sample, we study how the electron wind, which is a force on the ions in the lattice caused by momentum transfer from conduction electrons, affects the evolution of the microstructure. The corresponding simulation results presented in this thesis are unable to reproduce the precipitation mechanisms that have been reported in experimental studies of similar systems, which may indicate that the enhanced ageing process is caused by a different effect connected to the applied DC electric field. The thesis is concluded with final remarks and suggestions for future work.

Chapter 2

Aluminium alloys

This chapter presents information about the process of heat treating aluminium alloys in the 6xxx-series as a way of improving the properties of the alloys. We look at the precipitation sequence in these Al−Mg−Si alloys, and since this thesis studies the β'' precipitates, we talk about the structure and shape of these precipitates.

2.1 Precipitation hardening

The principal alloying elements in the 6xxx-series alloys are magnesium (Mg) and silicon (Si), and the contents of these solutes in the alloys are in the range of 0.5 wt% to 1.2 wt%, where the ratio Si/Mg is usually larger than one [17, 18]. The alloys may also contain other alloying elements, either trace elements from the extraction process of aluminium from alumina or elements added to the solution to enhance the properties of the alloys. In order to obtain higher strength of the Al−Mg−Si alloys, they are heat treated, and the corresponding strengthening mechanism is often referred to in the literature as precipitation hardening or age hardening [19]. The heat treatment process causes the formation of precipitate phases in the microstructure of the alloys, and these precipitates strengthen the alloys. The increase in strength is caused by misfit strain between the precipitates and the surrounding aluminium host matrix, making the strength of the alloys dependent on the volume fraction of the precipitates [20].

A typical temperature graph of the heat treatment process of Al−Mg−Si alloys is shown in Fig. 2.1. The process begins by heating the alloy sample to a temperature below the melting temperature for aluminium where the solutes dissolve into the Al matrix. This temperature depends on which alloying elements are found in the sample, and is usually above 450 °C [21]. By heating the sample, the solute atoms distribute close to uniformly in the microstructure and make the system into a single-phase solid solution. The next step is to rapidly cool the sample down to room temperature using a method known as water quenching, which is performed by submerging the sample in a water bath. This method is used to reduce the formation of precipitates during the cooling process down to room temperature, making the sample a supersaturated solid solution (SSSS).

This state is unstable and leaves the system with a large number of vacancies in the microstructure, which increases the diffusion of the solute atoms and results in the formation of solute clusters [19]. Leaving the sample at room temperature continues the formation of solute clusters, which grow into Guinier-Preston zones (GP zones), causing the hardness of the macroscopic sample to slowly increase

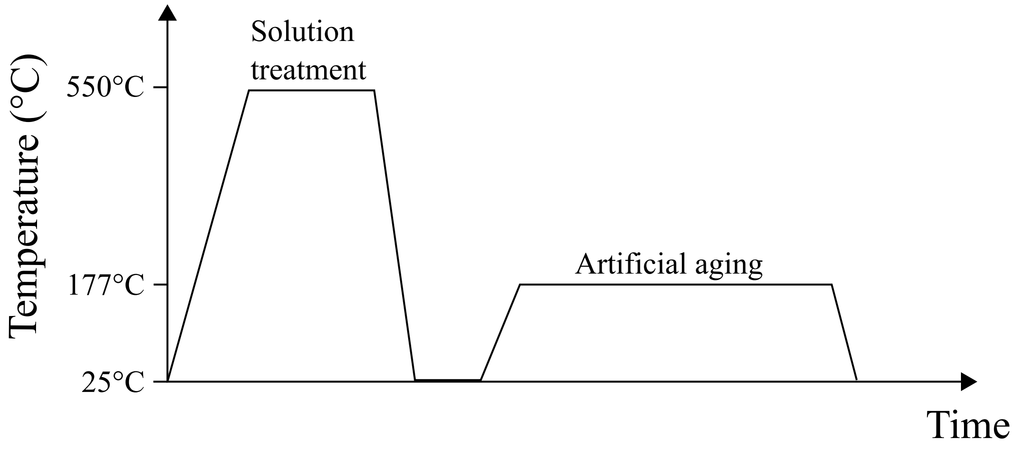

Figure 2.1. *Typical heat treatment process for* Al–Mg–Si *alloys with artificial ageing. The sample is first heated to* 550 °C*, so that the alloying elements dissolve into the* Al *matrix. The sample is then rapidly cooled down to room temperature, making the sample a supersaturated solid solution. At this point, solute clusters begin forming in the microstructure of the alloy, and the alloy is naturally aged at room temperature for a brief time interval. To artificially age the sample, it is heated and held at* 177 °C *during the ageing time.*

[4]. This method is known as natural ageing, but it does not give the sample the desired hardness. To achieve the peak strength, the sample is heated up to a temperature in the range of 150 °C to 180 °C after a brief time of natural ageing, and this method is known as artificial ageing. During the ageing time, the solute clusters may go through several structural phase transformations before reaching an equilibrium phase. The precipitation sequence for Al−Mg−Si alloys has been investigated extensively by many researchers, and they agree on the precipitation of the following precipitates (some introduce additional precipitate phases) [4, 19, 20, 22]

$$\text{SSSS} \rightarrow \text{solute clusters} \rightarrow \text{GP zones} \rightarrow \beta'' \rightarrow \beta' \rightarrow \beta.$$

β'' and β' are metastable, semi-coherent precipitates, while β is the equilibrium precipitate. The maximum hardness of the Al−Mg−Si alloys is reached when the alloys contain a combination of GP zones and β'' precipitates [23], which is the reason why we consider the precipitation of β'' precipitates in this thesis.

2.2 Microstructure of Al-Mg-Si alloys

The crystal structure of pure aluminium is given by a face-centred cubic (FCC) lattice. When an aluminium alloy sample with a low percentage of alloying elements is in a supersaturated solid solution during the heat treatment process, the crystal structure is assumed to be close to FCC [24]. When the formation of precipitates begins, the crystal structures of these precipitates are often different from the Al matrix because those structures are energetically favourable for the bulk of the precipitates. However, the difference in the crystal structure at the phase boundary between the precipitates and the Al matrix causes misfit strain effects on the precipitates.

Due to the misfit strain on the β'' precipitates, they are shaped as fine needles of typical dimensions $4 \times 4 \times 50\,\text{nm}^3$ when the sample is age-hardened [23]. This shape can be seen in the bright-field TEM image of a naturally aged sample of aluminium alloy 6082 in Fig. 2.2. From this TEM image, the precipitates are also seen to be oriented in three different spatial orientations. One of these orientations is in the plane, making the precipitates look like dark spots.

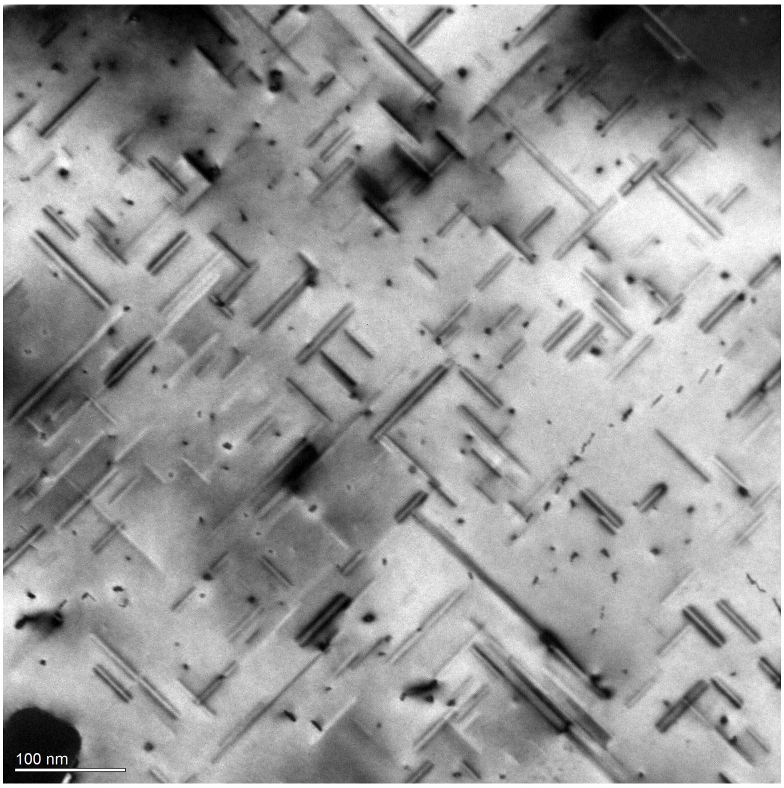

Figure 2.2. *A bright-field TEM image of a sample of aluminium alloy 6082 which has been aged naturally at* 0 ℃ *for a month, showing needle-shaped* β'' *precipitates. This image was provided by Petter Lervik, M.Sc. student at NTNU Gløshaugen, Department of Physics.*

The β'' precipitates are metastable and cannot exist outside the Al host matrix, and this makes it more difficult to study their structure and physical properties. The atomic structure of β'' precipitates has been studied extensively using several experimental techniques, and this has led to different reports of the atomic contents in this phase [23, 25]. In this thesis, we consider the structure of the β'' precipitates to be Mg_5Si_6, which has a monoclinic crystal structure.

Previous experimental studies have applied different types of external fields across alloy samples in order to study how the fields affect the precipitation during the ageing process and the peak properties of the samples. These studies have shown that the application of an external field, often an electrostatic or electric current field, can decrease the ageing time and give higher peak values for material properties such as hardness and conductivity for some alloys [7, 9]. Several explanations of how an applied electric field affects the microstructure evolution have been presented, hypothesizing that the applied electric field distributes the precipitates more homogeneously and with higher volume fractions, and that the field causes a higher diffusion rate of the solute atoms [10, 26]. It has also been discussed that the survival time of vacancies might be increased for samples aged in an applied field, which may increase the number density of nucleation sites in the microstructure.

Chapter 3

Phase-field modelling

In order to simulate the microstructural evolution of an Al−Mg−Si alloy during artificial ageing, we define a phase-field model for a two-phase mixture of Mg_5Si_6 precipitate (β'') in an aluminium host matrix, including the incorporation of nucleation, elastic strain and the electron wind caused by an applied direct current. The model is based upon a thermodynamic formulation, where the system evolves by minimising the total free energy of the system, moving the state of the system towards thermodynamic equilibrium. The phase-field approach has been found to be advantageous for modelling the microstructural evolution of alloys because it gives an efficient way of solving phase boundary problems by modelling the interface between phases as diffuse [15]. For sharp-interface models, the position of the interfaces needs to be tracked using mathematical equations during the temporal evolution of the system. Meanwhile, by using the diffuse-interface approach, there is no need to track the interfaces, as they are given implicitly through the evolution of the phase-field variables [12].

The problem with the phase-field method is that it is difficult to obtain quantitative results from the simulations. Firstly, some of the parameters that are used in the phase-field equations are difficult to measure for real alloys. Secondly, by modelling the interface width as significantly larger than for real alloys, the contribution from the interfaces to the evolution of the system will differ from the microstructural evolution in real alloys. Meanwhile, attempting to make the interfaces sharper increases the computational cost of solving the phase-field equations at the interfaces, due to the rapidly changing phase-field variables in these regions.

The phase-field equation for solving the temporal evolution of a given phase-field variable depends on whether the variable is conserved or non-conserved. The evolution of conserved phase-field variables is governed by the Cahn-Hilliard equation, while the evolution of non-conserved phase-field variables is governed by the Allen-Cahn (time-dependent Ginzburg-Landau) equation [27, 28]. In this thesis, we consider a conserved phase-field variable, and thus the main equation in our model is the Cahn-Hilliard equation. The Cahn-Hilliard equation is also modified to take into account the contributions from elastic strain and the electron wind.

3.1 The Cahn-Hilliard equation

In the following, we derive the Cahn-Hilliard equation for a two-component system, where the system is described by a conserved phase-field variable c, which represents the composition field of one of the components. The total free energy of the system is given as

$$F = F_{\text{bulk}} + F_{\text{int}} + F_{\text{other}}, \tag{3.1}$$

where F_{bulk} is the chemical free energy of the bulk, F_{int} is the interfacial free energy from the phase boundaries, while F_{other} accounts for additional free energy terms. Later, the contribution from elastic strain and the electron wind is implemented into the F_{other} term, but for now, we only consider the two first terms. In this case, the total free energy can be expressed as the functional

$$F\left[c\right] = \int_{\Omega} f_{\text{loc}}\left(c\right) + \frac{\kappa}{2}\left|\nabla c\right|^2 \mathrm{d}^3\mathbf{r}, \tag{3.2}$$

where f_{loc} is the local free energy density and κ is a gradient energy coefficient. The function $f_{\text{loc}}\left(c\right)$ has the shape of a double-well, similar to the graph shown in Fig. 3.1, giving two equilibrium compositions denoted by $c_{\text{eq},\alpha}$ and $c_{\text{eq},\beta}$.

In general, the gradient energy coefficient depends on the crystal symmetry of the system and is given by the tensor κ_{ij}, but in this thesis we assume that the gradient energy coefficient is isotropic, giving

$$\kappa_{ij} = \begin{cases} \kappa & \text{for } i = j, \\ 0 & \text{for } i \neq j. \end{cases}$$

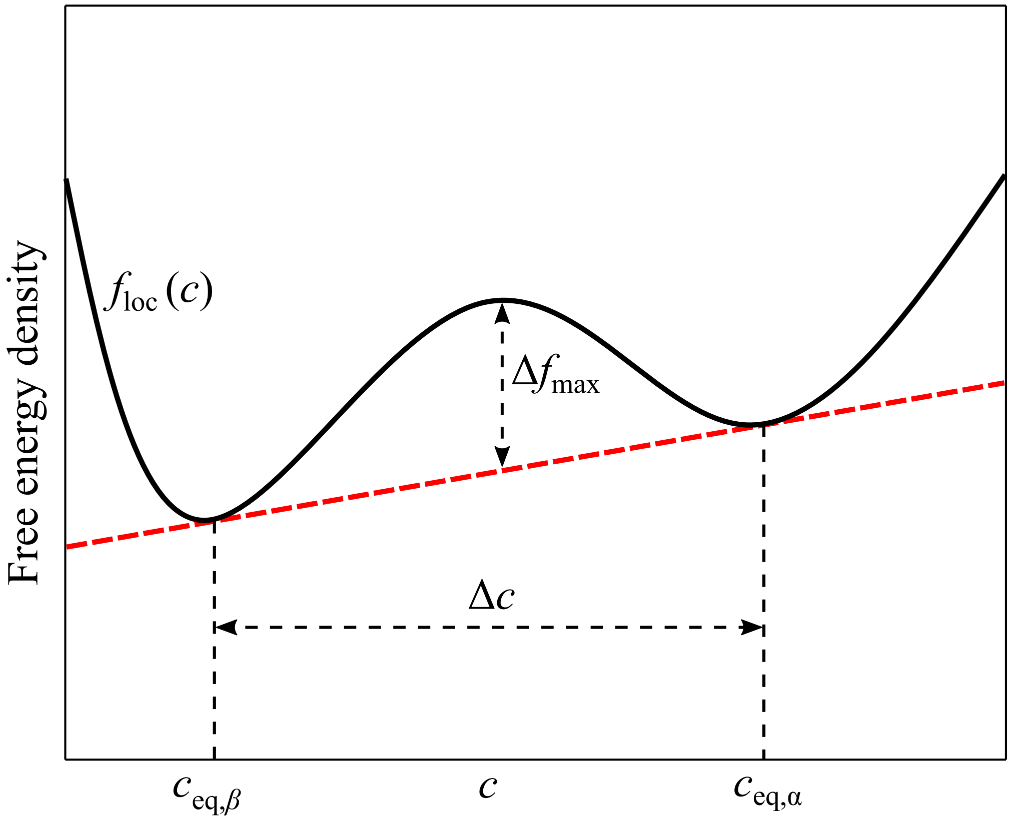

Figure 3.1. *Double-well shaped $f_{\text{loc}}(c)$, giving two equilibrium compositions.*

The interfacial free energy is expressed through the gradient of c, and since the total surface energy is independent of κ, that means that κ determines the diffuseness of the interface profile. The interface thickness l can be calculated from the formula [27]

$$l = \Delta c \sqrt{\frac{\kappa}{\Delta f_{\text{max}}}}. \tag{3.3}$$

Here, Δc is the difference between the two equilibrium compositions of the f_{loc} expression and Δf_{max} is the height of the barrier between the two wells above the tangent through the equilibria, as shown in Fig. 3.1.

Since the composition field c is a conserved field variable, it must follow a continuity equation of the form

$$\frac{\partial c}{\partial t} = -\nabla \cdot \mathbf{j}, \tag{3.4}$$

where $\mathbf{j}$ is the flux of c, which is related to the driving force for the chemical diffusion of the composition field. This driving force is connected to the chemical potential μ through the expression

$$\mathbf{F}_{\mathrm{chem}} = -\nabla\mu, \tag{3.5}$$

where the chemical potential is defined as the functional derivative of the total free energy

$$\mu = \frac{\delta F\left[c\right]}{\delta c}. \tag{3.6}$$

From this, the flux can be expressed as

$$\mathbf{j} = M\left(c\right)\mathbf{F}_{\mathrm{chem}} = -M\left(c\right)\nabla\frac{\delta F\left[c\right]}{\delta c}, \tag{3.7}$$

where $M\left(c\right)$ is the mobility of the composition field. By inserting this expression for $\mathbf{j}$ into Eq. 3.4, we get the Cahn-Hilliard equation [27]

$$\frac{\partial c}{\partial t} = \nabla M\left(c\right)\nabla\frac{\delta F\left[c\right]}{\delta c}. \tag{3.8}$$

Considering the functional

$$G\left[\rho\left(\mathbf{r}\right)\right] = \int g\left(\mathbf{r}, \rho\left(\mathbf{r}\right), \nabla\rho\left(\mathbf{r}\right), \nabla^2\rho\left(\mathbf{r}\right), \ldots, \nabla^N\rho\left(\mathbf{r}\right)\right) \mathrm{d}^3\mathbf{r},$$

the general formula for calculating the functional derivative is [29, pp. 248]

$$\frac{\delta G\left[\rho\right]}{\delta\rho} = \frac{\partial g}{\partial\rho} + \sum_{i=1}^{N}\left(-1\right)^i\nabla^i\cdot\frac{\partial g}{\partial\left(\nabla^i\rho\right)}.$$

In the case of the free energy functional $F\left[c\right]$, this functional is only dependent on c and ∇c, and thus the functional derivative becomes

$$\frac{\delta F\left[c\right]}{\delta c} = \frac{\partial f_{\mathrm{loc}}}{\partial c} - \kappa\nabla^2 c.$$

By inserting this expression into Eq. 3.8, we obtain the Cahn-Hilliard equation for our model as the fourth-order partial differential equation

$$\frac{\partial c}{\partial t} = \nabla M\left(c\right)\nabla\left[\frac{\partial f_{\mathrm{loc}}}{\partial c} - \kappa\nabla^2 c\right], \tag{3.9}$$

giving the temporal evolution of the composition field c.

Considering the energy minimisation of Eq. 3.2 and by looking at Fig. 3.1, we can expect three different cases of evolution for the composition field depending on the average composition c_{avg} in the system. We denote compositions close to $c_{\mathrm{eq},\beta}$

as β-phase and compositions close to $c_{\text{eq},\alpha}$ as α-phase. The first case is given by $c_{\text{avg}} \leq c_{\text{eq},\beta}$ or $c_{\text{avg}} \geq c_{\text{eq},\alpha}$, and here we expect the system to only have one phase, as it would not be energetically favourable for the composition field to decompose into two phases. The second and third cases are related to the turning points of f_{loc}, which are found by solving

$$\frac{\partial^2 f_{\text{loc}}}{\partial c^2} = 0. \tag{3.10}$$

We denote the two turning-point compositions, which are located on the barrier between the two wells, as $c_{\text{turn},\beta}$ and $c_{\text{turn},\alpha}$. The second case is found for $c_{\text{avg}} \in [c_{\text{turn},\beta}, c_{\text{turn},\alpha}]$. In this interval, we can see from Fig. 3.1 that the free energy density function has negative curvature ($\partial^2 f_{\text{loc}}/\partial c^2 < 0$), making the system unstable. Consequently, the system is expected to spontaneously separate into two phases, where the compositions of the phases move towards the equilibrium compositions. This evolution mechanism is known as spinodal decomposition [30].

The third case is found between the intervals of the first and second case in the regions $c_{\text{avg}} \in [c_{\text{eq},\beta}, c_{\text{turn},\beta}]$ and $c_{\text{avg}} \in [c_{\text{turn},\alpha}, c_{\text{eq},\alpha}]$. Here, the free energy density function has positive curvature, which means that phase separation will not occur spontaneously. However, separating the composition field into two phases is beneficial for minimising the total free energy of the system. This can be achieved through nucleation, which is a mechanism where larger fluctuations in the composition field lead to the formation of the second phase. Most alloys are described either by the first or the third case, depending on the temperature of the alloy. In this thesis, we mainly consider systems where nucleation is needed to achieve phase separation, but we also look at systems where the evolution is driven by spinodal decomposition to test our phase-field model. We introduce the nucleation model used in this thesis in Chapter 4.

The evolution of the microstructure is as previously mentioned driven by minimising the total free energy of the system. Since no anisotropic terms have been introduced into our phase-field model, as κ is chosen to be isotropic, the precipitates that evolve in the second and third cases described above are expected to be shaped like circles or stripes, as these shapes minimise the interfacial area, and thus the interfacial energy. Another expectation for the microstructural evolution is that the number of precipitates decreases, while the remaining precipitates grow larger. This coarsening process is driven by two evolution mechanisms. Firstly, smaller precipitates have higher interfacial energies than larger precipitates per area of the precipitate, which causes the smaller precipitates to dissolve so that the solute atoms can accumulate on the larger precipitates. This mechanism is known as Ostwald ripening [31]. In addition to this mechanism, the precipitates can also merge if they come close to each other.

3.2 Implementing additional contributions into the model

We expand our model by implementing the contributions from an applied direct current (DC) electric field to the evolution of the composition field c through introducing an additional term into the Cahn-Hilliard equation in Eq. 3.9. We also implement the contributions from elastic strain due to the misfit between the unit cells of the two components in the system. The addition of elastic strain on the precipitates is expected to change the stable shape of the precipitates, as the misfit and stiffness tensors are of anisotropic nature. In addition to studying the effects of adding these contributions into the system, we briefly look at the impact of allowing the temperature in the microstructure to fluctuate during the temporal evolution of the system.

When looking at the fluctuations in temperature, it would be possible to model the effects of Joule heating connected to the formation of precipitates. However, in this thesis we choose to model the temperature by the simple diffusion equation

$$\frac{\partial T}{\partial t} = \nabla D_T \nabla T, \tag{3.11}$$

where D_T is the thermal diffusivity of the material. We then look at the temperature evolution from an initial condition defined by a high-temperature and a low-temperature region in the system.

3.2.1 Applying a DC electric field

The evolution of the system defined in Section 3.1 is only driven by chemical diffusion. We now apply a direct current across the system, and consider the evolution to be driven by chemical diffusion and electromigration, also known as electron wind. Electromigration is the diffusion of ions caused by momentum transfer from conduction electrons to ions in an applied current [32]. The current $\mathbf{J}$ can be expressed by the electric potential V as

$$\mathbf{J} = \sigma\left(c\right)\mathbf{E} = -\sigma\left(c\right)\nabla V,$$

where $\mathbf{E}$ is the electric field and $\sigma\left(c\right)$ is the electrical conductivity. The electric current is governed by the Laplace equation, and thus the equation for the electric potential becomes

$$\nabla\left(\sigma\left(c\right)\nabla V\right) = 0. \tag{3.12}$$

The force exerted by the electrostatic field and the electron wind onto a unit volume is modelled as the force on the effective valence electrons of the atoms in the volume. This can be expressed as [33]

$$\mathbf{F}_{\text{elec}} = N_a\left|e\right|Z^*\nabla V,$$

where $N_a\left|e\right|Z^*$ is the effective valence electron density. Here, N_a is the number of atoms per unit volume, e is the electric charge of an electron and Z^* is the effective valence of the atoms. This driving force can be combined with the driving force for the chemical diffusion of c from Eq. 3.5, and then inserted into the expression for the flux $\mathbf{j}$ in Eq. 3.7, giving

$$\mathbf{j} = -M\left(c\right)\left[\nabla\frac{\delta F\left[c\right]}{\delta c} - N_a\left|e\right|Z^*\nabla V\right].$$

From this new expression for the flux of the composition field, we obtain the modified Cahn-Hilliard equation accounting for the contribution from the DC electric field [34]

$$\frac{\partial c}{\partial t} = \nabla M\left(c\right)\nabla\left[\frac{\partial f_{\text{loc}}}{\partial c} - \kappa\nabla^2 c - N_a\left|e\right|Z^* V\right]. \tag{3.13}$$

3.2.2 Modelling the contributions from elastic strain

We continue by modelling the contributions from elastic strain on the system due to misfit strain, which is expected to affect the shape of the precipitates in the composition field. When modelling the elastic contributions into the phase-field model, we need the elastic stress, strain, stiffness tensor and elastic energy, and there exist several different schemes for modelling these quantities in phase-field models. The most commonly used scheme is the Khachaturyan scheme [35, 36], which is the scheme we use in this thesis to implement the elastic strain effects into our phase-field model. This scheme models the stiffness tensor and misfit strain as functions of the phase-field variable and assumes linear elasticity.

To couple the elastic strain to the phase-field model, we add the elastic strain energy into F_{other} in Eq. 3.1. Assuming that there is no applied stress on the system, the Khachaturyan scheme models the elastic free energy in terms of the stiffness tensor C_{ijkl} and the elastic strain tensor $\epsilon_{ij}^{\text{el}}$ as [15]

$$F_{\text{strain}} = \int_V \frac{1}{2} C_{ijkl}\left(c\right) \epsilon_{ij}^{\text{el}}\left(\mathbf{r}\right) \epsilon_{kl}^{\text{el}}\left(\mathbf{r}\right) \mathrm{d}^3\mathbf{r}.$$

Here, the stiffness tensor is modelled to equal the individual stiffness tensor of the corresponding phase at the equilibrium compositions, giving

$$C_{ijkl}\left(c\right) = C_{ijkl,\beta} \frac{c_{\text{eq},\alpha} - c}{c_{\text{eq},\alpha} - c_{\text{eq},\beta}} + C_{ijkl,\alpha} \frac{c - c_{\text{eq},\beta}}{c_{\text{eq},\alpha} - c_{\text{eq},\beta}}, \tag{3.14}$$

where $c_{\text{eq},\alpha/\beta}$ are the equilibrium compositions from Fig. 3.1. The elastic strain is defined as the difference between the total strain $\epsilon_{ij}^{\text{tot}}\left(\mathbf{r}\right)$ and the inelastic strain, which in our case is the misfit strain $\epsilon_{ij}^{0}\left(c\right)$, giving

$$\epsilon_{ij}^{\text{el}}\left(c\right) = \epsilon_{ij}^{\text{tot}} - \epsilon_{ij}^{0}\left(c\right). \tag{3.15}$$

To determine the total strain on a unit volume, we introduce the displacement field $\mathbf{u}\left(\mathbf{r}\right)$ and use the assumption of linear elasticity in the system, which is common for phase-field modelling of precipitation in alloys [35, 37]. The assumption of linear elasticity assumes that the gradient of the displacement, $\nabla\mathbf{u}$, is smaller than unity, and thus the squared displacement gradient term is neglected. This gives the total elastic strain tensor as [38]

$$\epsilon_{ij}^{\text{tot}} = \frac{1}{2}\left(\frac{\partial u_j}{\partial x_i} + \frac{\partial u_i}{\partial x_j}\right).$$

The misfit strain originates from the difference between the stress-free lattices of the two components, which in our case are the FCC Al and the monoclinic $\mathrm{Mg_5Si_6}$. To express the misfit strain, we need the matrix that transforms the stress-free unit cell of Al into the unit cell of $\mathrm{Mg_5Si_6}$. By defining the unit cell matrices

$$\mathbf{U}_{\mathrm{Al}} = \begin{bmatrix} \mathbf{a}_{\mathrm{Al}} & \mathbf{b}_{\mathrm{Al}} & \mathbf{c}_{\mathrm{Al}} \end{bmatrix} \quad , \quad \mathbf{U}_{\mathrm{Mg_5Si_6}} = \begin{bmatrix} \mathbf{a}_{\mathrm{Mg_5Si_6}} & \mathbf{b}_{\mathrm{Mg_5Si_6}} & \mathbf{c}_{\mathrm{Mg_5Si_6}} \end{bmatrix},$$

where $\mathbf{a}, \mathbf{b}$ and $\mathbf{c}$ are the lattice vectors of the unit cell for the specified component, we can find the transformation matrix $\mathbf{P}$ from

$$\mathbf{U}_{\mathrm{Mg_5Si_6}} = \mathbf{P}\mathbf{U}_{\mathrm{Al}}. \tag{3.16}$$

The misfit strain between the two components can then be expressed by the formula [14, 39]

$$\epsilon^0_{ij} = \frac{1}{2}\left(\mathbf{P}^\top \mathbf{P} - \mathbb{I}\right), \tag{3.17}$$

where $\mathbb{I}$ is the identity matrix. Misfit strain is by definition nonzero inside the precipitates and zero outside the precipitates [35], and for this reason, the misfit strain is modelled as

$$\epsilon^0_{ij}\left(c\right) = \epsilon^0_{ij}\frac{c - c_{\mathrm{eq},\beta}}{c_{\mathrm{eq},\alpha} - c_{\mathrm{eq},\beta}}. \tag{3.18}$$

The final part needed for the implementation of the elastic effects is to calculate the displacement field $\mathbf{u}$, and this is accomplished by solving the mechanical equilibrium equation

$$\frac{\partial \sigma_{ij}}{\partial r_j} = 0, \tag{3.19}$$

where $\sigma_{ij}\left(\mathbf{r}\right)$ is the mechanical stress. Due to the assumption of linear elasticity in the Khachaturyan scheme, this stress is related to the elastic strain through Hooke's law as [35]

$$\sigma_{ij}\left(\mathbf{r}\right) = C_{ijkl}\left(c\right)\epsilon^{\mathrm{el}}_{kl}\left(\mathbf{r}\right) = C_{ijkl}\left(c\right)\left(\epsilon^{\mathrm{tot}}_{kl}\left(\mathbf{r}\right) - \epsilon^0_{kl}\frac{c\left(\mathbf{r}\right) - c_{\mathrm{eq},\beta}}{c_{\mathrm{eq},\alpha} - c_{\mathrm{eq},\beta}}\right),$$

where we used Eqs. 3.15 and 3.18. Now, we have implemented all the contributions we want to study in this thesis into our phase-field model.

3.3 System spesifications

The phase-field model we have presented in Sections 3.1 and 3.2 could be applied to any two-phase alloy system since no assumptions have been made regarding the microstructure of the system. In this section, we determine a local free energy density expression and the necessary parameters for our 6xxx-series aluminium alloy system. As previously mentioned, β'' precipitates are metastable and cannot exist outside the aluminium host matrix, which makes it difficult to measure the values of some of the physical properties such as electrical conductivity for these structures. For this reason, some of the parameters are chosen to be the values for pure aluminium, as these values are expected to be of the same order of magnitude as the exact values of the alloys. Due to these parameter choices and the qualitative nature of the phase-field method, the results in this thesis are analysed in a qualitative matter. By this, we mean that the thesis studies the mechanisms in the microstructure evolution, while not looking for exact values of properties such as the hardness of the macroscopic alloy sample. We begin by determining an expression for the local free energy density $f_{\text{loc}}(c)$ in Eq. 3.2.

3.3.1 Determining a free energy density expression

The local free energy density used in phase-field models is usually expressed as a Landau polynomial of the phase-field variables [15]. In our case, the only phase-field variable we consider is the composition field c, which represents the amount of Mg_5Si_6 in the system. To begin with, we wanted to fit free energy data from a thermodynamic database for a 6xxx-series aluminium alloy to a polynomial of the form

$$f_{\text{loc}} = f_0 + Ac + B(T)c^2 + Cc^4.$$

We attempted to do this using the CALculation of PHAse Diagrams (CALPHAD) method, but this proved difficult as Mg_5Si_6 is an intermetallic compound, leading to the free energy of this phase only being defined at a single concentration.

Instead, we chose to model the local free energy density as the Landau polynomial

$$f_{\text{loc}}\left(c,T\right)=A\frac{T-T_{\text{c}}}{T_{\text{c}}}c^{2}+Bc^{4}, \tag{3.20}$$

where T_{c} is a critical temperature and the coefficients A and B are determined using thermodynamic relations. This function is a symmetric double-well about $c=0$ for $T<T_{\text{c}}$, and the stable equilibrium compositions c_{eq} can be found by solving $\partial f_{\text{loc}}(c_{\text{eq}})/\partial c=0$, giving

$$c_{\text{eq}}=\pm\sqrt{-\frac{A}{2B}\frac{T-T_{\text{c}}}{T_{\text{c}}}}. \tag{3.21}$$

We imposing two qualitative restrictions on the system to be able to determine the coefficients. Firstly, the composition field is restricted to the interval $c\in(-1,1)$ for all temperatures T. Secondly, the stable equilibrium compositions c_{eq} move towards ±1 as $T\to 0\,\text{K}$. We may also note that the two stable equilibrium compositions coincide at $c=0$ for $T>T_{\text{c}}$, giving a single-phase system for temperatures above the critical temperature. By considering the system where $T\to 0\,\text{K}$ and inserting $c_{\text{eq}}=\pm 1$ into Eq. 3.21, we find the relationship $A=2B$. Consequently, this gives the equilibrium compositions as

$$c_{\text{eq}}=\pm\sqrt{\frac{T_{\text{c}}-T}{T_{\text{c}}}} \tag{3.22}$$

for all $T<T_{\text{c}}$.

All that remains is to determine the value of B. This coefficient could be determined in many different ways, but we choose to connect it to the heat capacity. The volumetric heat capacity is connected to the free energy density through the thermodynamic relation

$$C_v=-T\frac{\partial^2 f_{\text{loc}}}{\partial T^2}.$$

By using the expression for the equilibrium compositions in Eq. 3.22 and introducing the reduced temperature $t=(T-T_{\text{c}})/T_{\text{c}}$, we get

$$f_{\text{loc}}\left(c_{\text{eq}}\left(t\right),t\right)=B\left(-2t^2+t^2\right)=-Bt^2.$$

The thermodynamic relation for the volumetric heat capacity can be expressed with the reduced temperature by using

$$\frac{\partial}{\partial T}=\frac{1}{T_{\text{c}}}\frac{\partial}{\partial t},$$

giving the volumetric heat capacity as

$$C_v = -\frac{T}{T_{\mathrm{c}}^2}\frac{\partial^2 f_{\mathrm{loc}}}{\partial t^2} = \frac{2BT}{T_{\mathrm{c}}^2}.$$

We choose to consider the reference temperature $T_{\mathrm{ref}} = 298\,\mathrm{K}$ (room temperature), where the volumetric heat capacity is found to be $C_{v,\mathrm{ref}} = 0.0151\,\mathrm{eV/nm^3K}$ by multiplying the specific heat capacity of aluminium with the density of aluminium [40]. Here, we neglected the impact of the alloying elements on the specific heat capacity and density, as we expect the corresponding values for 6xxx-series alloys to be of the same order of magnitude as for pure aluminium. By using these reference values, the coefficient B is expressed as

$$B = \frac{C_{v,\mathrm{ref}} T_{\mathrm{c}}^2}{2T_{\mathrm{ref}}},$$

and by substituting this into Eq. 3.20, we obtain the free energy density expression

$$f_{\mathrm{loc}}\left(c, T\right) = \frac{C_{v,\mathrm{ref}} T_{\mathrm{c}}^2}{2T_{\mathrm{ref}}}\left(2\frac{T - T_{\mathrm{c}}}{T_{\mathrm{c}}}c^2 + c^4\right). \tag{3.23}$$

It is now interesting to investigate whether the phase-field variable c can be considered as the molar fraction of $\mathrm{Mg_5Si_6}$ in the system defined by this free energy density expression for the binary $\mathrm{Al{-}Mg_5Si_6}$ system. In order to consider this, we look at the phase fraction and aluminium content of the FCC aluminium phase for a system defined by molar fractions corresponding to real values for 6xxx-series aluminium alloys. The phase fraction of a binary solution can be found for a given total composition c_{tot} by minimising

$$G\left(c_\alpha, c_\beta, f\right) = fG_\alpha\left(c_\alpha\right) + \left(1 - f\right)G_\beta\left(c_\beta\right)$$

with respect to c_α, c_β and f, given the restriction

$$c_{\mathrm{tot}} = fc_\alpha + \left(1 - f\right)c_\beta. \tag{3.24}$$

Here, c_α is the equilibrium composition of phase α, c_β is the equilibrium composition of phase β and f is the phase fraction of phase α. In our system, the α phase corresponds to the $\mathrm{Mg_5Si_6}$-rich phase, while the β-phase corresponds to the Al-rich phase. Our free energy density expression in Eq. 3.23 is symmetric about $c = 0$, giving $c_\alpha = -c_\beta = c_{\mathrm{eq}}$. We observe two cases depending on the value of c. As

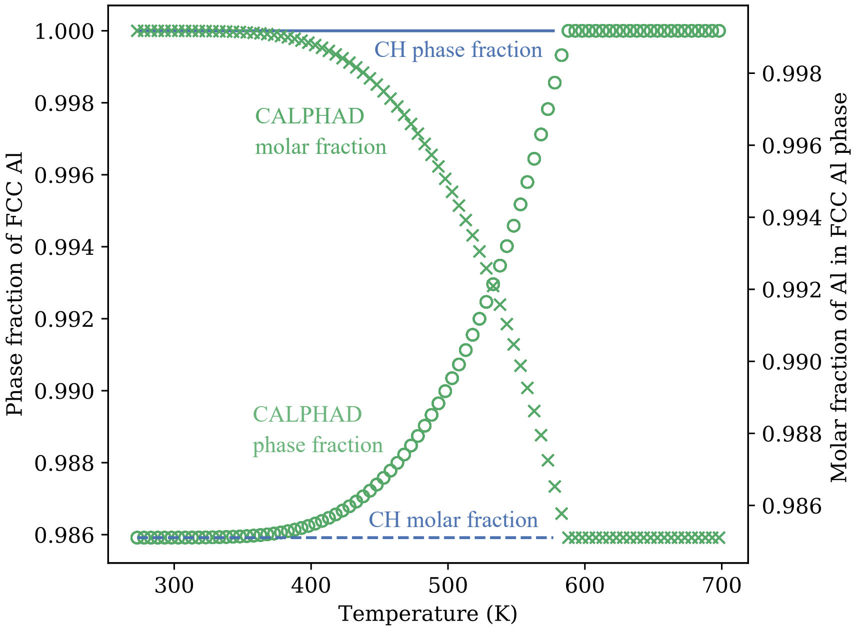

Figure 3.2. *The phase fraction of FCC* Al *phase and the molar fraction of* Al *in this phase as a function of temperature for a 6xxx-series aluminium alloy containing* 98.5 mol% Al. *The blue lines, denoted by CH, were calculated using the free energy expression in Eq. 3.23, while the green markers, denoted by CALPHAD, were calculated using data from a thermodynamic database for a 6xxx-series alloy.*

discussed in Section 3.1, if $|c| > c_{\mathrm{eq}}$, we do not expect phase separation, and thus the free energy will minimise at $f = 0$ or $f = 1$ depending on whether c is closest to $-c_{\mathrm{eq}}$ or $+c_{\mathrm{eq}}$, respectively. Note that the composition of this single-phase will be given by c, and not c_{eq}. The other case is for $-c_{\mathrm{eq}} < c < c_{\mathrm{eq}}$, where we expect phase separation with the phases being given by compositions close to $\pm c_{\mathrm{eq}}$. By inserting $c_\alpha = -c_\beta = c_{\mathrm{eq}}$ into Eq. 3.24, we obtain the formula for the phase fraction of Mg_5Si_6 as

$$f = \frac{c + c_{\mathrm{eq}}}{2c_{\mathrm{eq}}},$$

and from this we get the phase fraction of FCC aluminium as $f_{\mathrm{Al}} = 1 - f$. Since real 6xxx-series aluminium alloys have an aluminium content above 95 mol%, we now look at a system containing 98.5 mol% Al. In Fig. 3.2, we have calculated the phase fraction and aluminium content in the FCC aluminium phase using both our free energy density expression and the CALPHAD method with a thermodynamic database for a 6xxx-series alloy. The calculation of the molar fraction using the free energy density expression was done by converting c onto the interval $[0,1]$ through the formula

$$c^* = \frac{c+1}{2}.$$

The CALPHAD calculations show that we get phase separation for temperatures up to approximately 580 K, while all Mg_5Si_6 has dissolved into the FCC aluminium phase above this temperature. It is therefore natural to consider this temperature as critical when considering precipitation in our alloy, and for this reason, we choose $T_\mathrm{c} = 580\,\mathrm{K}$ in our free energy expression. We can then notice that the phase fraction calculations using our free energy expression with this T_c give a single-phase system for all the temperatures in the range of 300 K to 580 K, and is thus in the case $|c| > c_\mathrm{eq}$. As a result, we consider c as a conserved order parameter in our phase-field model instead of trying to relate it to real molar

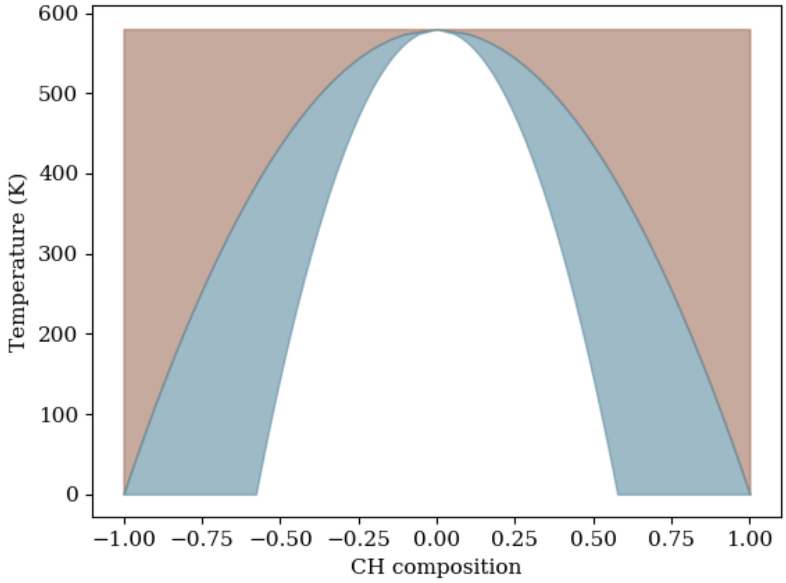

Figure 3.3. *The phase diagram for the* $Al{-}Mg_5Si_6$ *binary system, where CH composition denotes the phase-field variable c. The brown domain represents the stable region, giving a single-phase system. The blue domain represents the metastable region where nucleation gives phase separation, while the white domain represents the spinodal region where the system spontaneously separates into two phases.*

fractions, and the average value of c is chosen in order to obtain the precipitation phenomena we want to study.

Using our free energy density expression, we can make a phase diagram showing which case of microstructure evolution is expected for a given c_{avg} and T. As mentioned at the end of Section 3.1, the different cases are related to the equilibrium compositions and turning points of c. The equilibrium curve separating the single-phase and the two-phase region, also known as the binodal curve, is found by using Eq. 3.22. Meanwhile, the curve separating the spontaneous and non-spontaneous phase separation, often denoted as the spinodal curve, is found by solving Eq. 3.10 for our free energy expression. This results in the spinodal line defined by

$$c_{\text{spi}}\left(T\right) = \pm\sqrt{\frac{1}{3}\frac{T - T_{\text{c}}}{T_{\text{c}}}}.$$

The resulting phase diagram can be seen in Fig. 3.3, and we note that the system we considered when looking at the phase fraction of FCC aluminium above, correlating to $c = -0.975$, enters the single-phase region at a very low temperature.

Since the artificial ageing process is carried out at temperatures in the range of 150 °C to 180 °C, we choose to consider a constant temperature $T = 177\,^{\circ}\text{C} = 450\,\text{K}$ in our simulations, except for the system where we allow temperature fluctuations. By looking at the phase diagram in Fig. 3.3 for this temperature, we choose to use $c_{\text{avg}} = -0.35$ when we add nucleation to the model, as the point $(c_{\text{avg}} = -0.35, T = 450\,\text{K})$ is located inside the blue region of the phase diagram. When considering a system driven by spinodal decomposition, we choose to use $c_{\text{avg}} = -0.10$, as this point lies inside the white region of the phase diagram.

3.3.2 Determining appropriate boundary conditions and parameter values

All that remains before we can start setting up the simulations is to determine the values and dependencies of the parameters introduced in Sections 3.1 and 3.2 and to choose appropriate boundary conditions for the field variables in our system. We choose to consider a two-dimensional system of dimensions $100 \times 100\,\text{nm}^2$, and because this system is very small in comparison to a macroscopic sample of

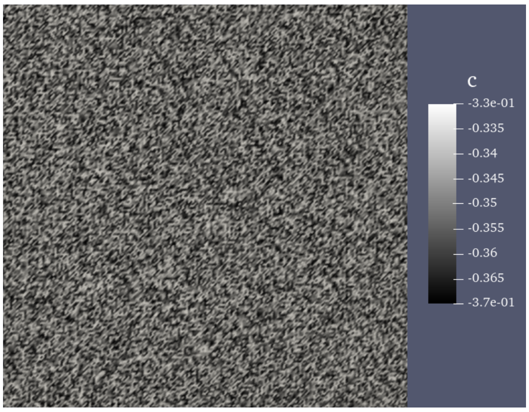

Figure 3.4. *Initial condition of the composition field for the nucleation system given by* $c \in [-0.37, -0.33]$.

aluminium alloy, we choose to apply periodic boundary conditions to c. Since the microstructure at the starting point of the ageing process in real alloys is described as a supersaturated solid solution, meaning that the components are approximately uniformly distributed in the sample, we define the initial condition of c by randomly distributed values close to the chosen c_{avg}. For the nucleation-driven system with $c_{\text{avg}} = -0.35$, the initial condition is defined by a random distribution in the interval $c \in [-0.37, -0.33)$ across the system, as shown in Fig. 3.4. Meanwhile, the initial condition for the spinodal system is given by a random distribution for $c \in [-0.12, -0.08]$.

When we apply a direct current across the system in the x-direction, we need to choose the boundary conditions for the potential V. Considering the direction of the current, we choose to apply periodic boundary conditions on V in the y-direction. However, we need to have a potential drop across the system in the x-direction, and therefore we define the system by Dirichlet boundaries $V = 0$ on the left side and $V = V_0$ on the right side of the system. We consider a potential drop across our system in the x-direction of $V_0 = 1 \times 10^{-2}\,\text{V}$, corresponding to an electric field of $1\,\text{kV/cm}$, as this value is of the same order of magnitude as the DC electric field in previous experimental studies [10].

One issue with defining the boundaries in this manner is that since the composition field is modelled using periodic boundaries, we get a discontinuity in the potential across the boundaries in the x-direction, which means that the potential over several repetitions of the system in the x-direction takes the shape of a sawtooth potential. This problem could be fixed by changing the boundary conditions of the composition field to either Dirichlet or Neumann conditions, but this change would have drawbacks too. If we choose Neumann conditions equal to zero, this would make it energetically favourable for the precipitates to locate themselves at the boundaries, as that would reduce the interfacial area between the precipitates and the host matrix, and thereby reduce the interfacial energy. This would also make the total area of the precipitates, which is a quantity we want to study in our simulations, increase compared to a system with periodic boundaries.

Meanwhile, if we consider the possibility of using Dirichlet boundaries, it would be natural to set these equal to the equilibrium concentration of the FCC Al phase, $-c_{\mathrm{eq}}$, to prohibit the formation of precipitates at the boundaries. This would solve the problem connected to the Neumann boundaries, but at the same time, it would interfere with the microstructure evolution of the system, especially early in the simulations when the compositions across the system are close to the chosen value of c_{avg}. Consequently, we choose to use periodic boundaries for c to let the microstructure evolve without being severely affected by the boundaries.

In the systems that take into consideration the elastic strain effects due to misfit between the phases, we want to study the preferred shape of the precipitates. In order to do that, we define a couple of initial conditions containing initial

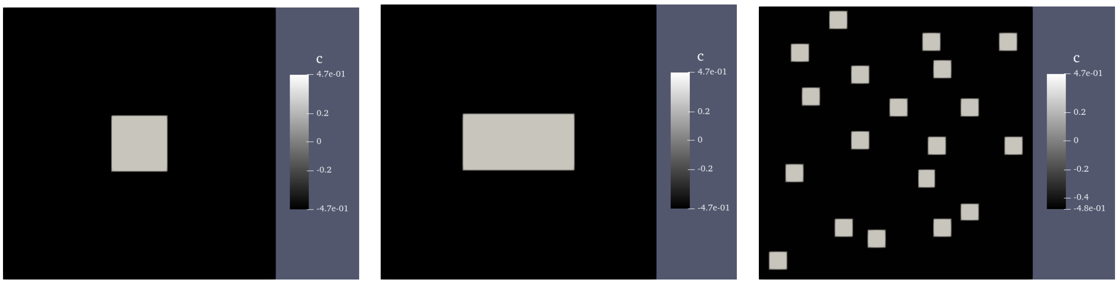

(a) (b) (c)

Figure 3.5. *Initial conditions for the systems containing elastic strain contributions.* (**a**) *Single square-shaped precipitate of dimensions* $20 \times 20\,\mathrm{nm}^2$*.* (**b**) *Single rectangular-shaped precipitate of dimensions* $40 \times 20\,\mathrm{nm}^2$*.* (**c**) *Multiple square-shaped precipitate of dimensions* $6 \times 6\,\mathrm{nm}^2$*.*

precipitates of different shapes and sizes. We consider the evolution of a single square-shaped precipitate of dimensions $20 \times 20\,\mathrm{nm}^2$, a single rectangular-shaped precipitate of dimensions $40 \times 20\,\mathrm{nm}^2$, and a system of several square-shaped precipitates of dimensions $6 \times 6\,\mathrm{nm}^2$. The precipitates are given by $c = c_{\mathrm{eq}}$, while $c = -c_{\mathrm{eq}}$ in the matrix around the precipitates, and the initial conditions can be seen in Fig. 3.5.

When we consider the possibility of temperature variations in the microstructure, we apply Neumann boundaries equal to zero, which makes the average temperature in the system conserved, since there are no heat sources or sinks in our model. In order to look at the temporal evolution of the temperature, we define the initial temperature as 450 K inside a circle of radius 25 nm in the centre of our system, while the temperature outside the circle is 300 K, as shown in Fig. 3.6. We use $D_T = 6.4 \times 10^{13}\,\mathrm{nm}^2/\mathrm{s}$ as the value for the thermal diffusivity, as this is a reported value for the thermal diffusivity of 6061-T6 aluminium alloy [41].

We proceed by defining the values and field variable dependencies of the parameters in our phase-field model, and we begin by modelling the mobility $M(c)$ in the Cahn-Hilliard equation. The mobility is modelled using several different expressions in the literature on phase-field modelling [12, 34, 36, 42], and we choose

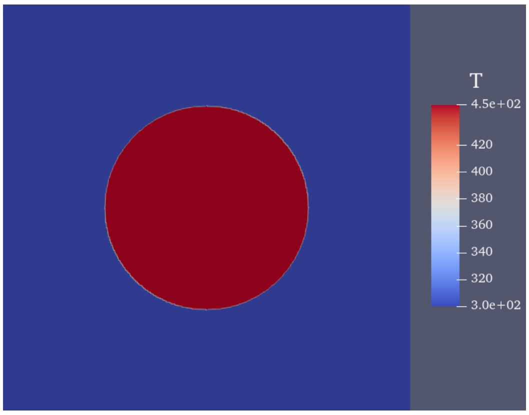

Figure 3.6. *Initial condition of the temperature field for the system allowing temperature fluctuations. The initial condition is given by* $T = 450\,\mathrm{K}$ *inside a circle in the centre of the system with a radius of* $25\,\mathrm{nm}$*, while* $T = 300\,\mathrm{K}$ *outside the circle.*

to model it as the simple expression

$$M(c) = M_0 \frac{(1-c)(1+c)}{4},$$

where M_0 is given by [12]

$$M_0 = \frac{DV_m}{RT}.$$

Here, D is the self-diffusion of aluminium, $V_m = 1.00 \times 10^{22}\,\mathrm{nm}^3/\mathrm{mol}$ is the molar volume of Al and R is the molar gas constant. Burke and Ramachandran [43] reported the self-diffusion of aluminium at 453 K to be $D = 7.95 \times 10^{-2}\,\mathrm{nm}^2/\mathrm{s}$, so we use this value for our system at $T = 450\,\mathrm{K}$. By inserting these values, we obtain $M_0 = 3.40 \times 10^{-2}\,\mathrm{nm}^5/\mathrm{eVs}$.

The value of the gradient energy coefficient κ determines how sharp or diffuse we model the interface between precipitates and the host matrix. Since precipitates in real alloys have sharp interfaces, we want to model the interfaces as sharp as possible, and therefore the choice of κ must be based on a consideration of the computational cost, in the sense that a finer mesh is needed at the interface regions for sharper interfaces in order to achieve satisfactory convergence in the calculations. Considering that our system is $100 \times 100\,\mathrm{nm}^2$, we found that an interface thickness $l = 2\,\mathrm{nm}$ gives reasonable computational cost while simultaneously giving sufficiently sharp interfaces to study the systems. By using Eq. 3.3, where $\Delta f_{\max} = 0.428\,\mathrm{eV}/\mathrm{nm}^3$ and $\Delta c = 2\,|c_{\mathrm{eq}}| = 0.947$ for our free energy density expression, we get $\kappa = 1.91\,\mathrm{eV}/\mathrm{nm}$.

We proceed by considering the parameters connected to the implementation of the DC electric field. The atomic density N_a in Eq. 3.13 is found by dividing the mass density by the molar mass. Once more, we use the values for pure aluminium to find this value, giving $N_a = \frac{2.70\times10^{-21}\,\mathrm{g/nm}^3}{27.0\,\mathrm{g/mol}} = 1 \times 10^{-22}\,\mathrm{mol/nm}^3 = 60.2\,\mathrm{atoms/nm}^3$. The effective valence is considered to be constant in the system with a value $Z^* = 4$. The electrical conductivity in Eq. 3.12 is modelled with a dependency on the composition field, $\sigma(c)$, leading to a difference between the electric field in the Al matrix and the precipitates. We model the electrical conductivity as a weighted average of the electrical conductivities of Al and Mg_5Si_6, expressed as

$$\sigma(c) = \sigma_{\mathrm{Al}} \frac{1-c}{2} + \sigma_{\mathrm{Mg_5Si_6}} \frac{1+c}{2}.$$

Since β'' precipitates cannot exist outside of the Al matrix, it is challenging to make accurate measurements of their electrical conductivity. By looking up the electrical conductivities of the elements Al, Mg and Si using the ElementData function from Wolfram Research [44], we find that the value of Si is several orders of magnitude smaller than for Al ($\sigma_{\mathrm{Al}} = 3.85 \times 10^{-2}\,\mathrm{S/nm}$, $\sigma_{\mathrm{Mg}} = 2.23 \times 10^{-2}\,\mathrm{S/nm}$, $\sigma_{\mathrm{Si}} = 1.00 \times 10^{-6}\,\mathrm{S/nm}$). As a result, we consider two ways of modelling the electrical conductivity of the $\mathrm{Mg_5Si_6}$ nuclei. First, we could approximate the conductivity $\sigma_{\mathrm{Mg_5Si_6}}$ to be zero, which would give the maximal effect of the contribution from the electron wind on the system. However, we instead model it as a weighted average of the electrical conductivities of the individual components, where the weights are given by the stoichiometric formula, giving

$$\sigma_{\mathrm{Mg_5Si_6}} = \frac{5\sigma_{\mathrm{Mg}} + 6\sigma_{\mathrm{Si}}}{11}.$$

By inserting the conductivity values from Wolfram Research [44], we obtain the electrical conductivity $\sigma_{\mathrm{Mg_5Si_6}} = 1.01\,\mathrm{S/nm}$.

Table 3.1. *Conversion of indices from a rank four tensor to a rank two tensor for Voigt notation.*

ij or kl	p or q
11	1
22	2
33	3
23=32	4
13=31	5
12=21	6

The parameters needed for the implementation of the elastic contributions are determined using the Khachaturyan scheme. We begin by considering the stiffness tensor $C_{ijkl}(c)$, which is found by inserting $c_{\mathrm{eq},\alpha} = -c_{\mathrm{eq},\beta} = c_{\mathrm{eq}}$ into Eq. 3.14. The stiffness tensors of the individual components are found at The Materials Project [45, 46], where the tensors have been calculated using density functional theory (DFT). The stiffness tensors can be represented by stiffness matrices using Voigt notation [47], where the indices ij and kl are replaced by p and q, respectively, following the index conversions in Table 3.1. This lets the stiffness matrix be represented by the symmetric 6 × 6 matrix

$$C_{ijkl} \rightarrow C_{pq} = \begin{bmatrix} C_{11} & C_{12} & C_{13} & C_{14} & C_{15} & C_{16} \\ C_{12} & C_{22} & C_{23} & C_{24} & C_{25} & C_{26} \\ C_{13} & C_{23} & C_{33} & C_{34} & C_{35} & C_{36} \\ C_{14} & C_{24} & C_{34} & C_{44} & C_{45} & C_{46} \\ C_{15} & C_{25} & C_{35} & C_{45} & C_{55} & C_{56} \\ C_{16} & C_{26} & C_{36} & C_{46} & C_{56} & C_{66} \end{bmatrix}.$$

The stiffness tensor for FCC Al is represented by the stiffness matrix [48]

$$C_{pq,\mathrm{Al}} = \begin{bmatrix} 104 & 73 & 73 & 0 & 0 & 0 \\ 73 & 104 & 73 & 0 & 0 & 0 \\ 73 & 73 & 104 & 0 & 0 & 0 \\ 0 & 0 & 0 & 32 & 0 & 0 \\ 0 & 0 & 0 & 0 & 32 & 0 \\ 0 & 0 & 0 & 0 & 0 & 32 \end{bmatrix},$$

where the unit of the matrix elements is GPa. Meanwhile, the stiffness tensor for monoclinic $\mathrm{Mg_5Si_6}$ is represented by the stiffness matrix [49]

$$C_{pq,\mathrm{Mg_5Si_6}} = \begin{bmatrix} 103 & 51 & 50 & 0 & -8 & 0 \\ 51 & 80 & 55 & 0 & 3 & 0 \\ 50 & 55 & 76 & 0 & 10 & 0 \\ 0 & 0 & 0 & 16 & 0 & 1 \\ -8 & 3 & 10 & 0 & 32 & 0 \\ 0 & 0 & 0 & 1 & 0 & 29 \end{bmatrix}.$$

The final parameter we need to calculate is the misfit strain tensor $\epsilon^0_{ij}(c)$, and hence we need the lattice vectors of the unit cells for the two components. The lattice parameters for the components are also reported in the data from The Materials Project, and these parameters can be used to find the lattice vectors. By orienting the conventional unit cell of the monoclinic $\mathrm{Mg_5Si_6}$ in the same direction with respect to the FCC Al as performed in Frafjord et al. [50], we obtain the unit cell matrix

$$\mathbf{U}_{\mathrm{Mg_5Si_6}} = \begin{bmatrix} 12.8 & -6.60 & 0 \\ 8.52 & 2.20 & 0 \\ 0 & 0 & 4.01 \end{bmatrix}.$$

The conventional unit cell of FCC Al gives the unit cell matrix

$$\mathbf{U}_{\mathrm{Al}} = \begin{bmatrix} 4.04 & 0 & 0 \\ 0 & 4.04 & 0 \\ 0 & 0 & 4.04 \end{bmatrix},$$

but we need the unit cells to be of approximately equal sizes. To achieve this, we need to multiply $\mathbf{U}_{\mathrm{Al}}$ by the integer matrix $\mathbf{S}$ that minimises the Frobenius norm $||\mathbf{U}_{\mathrm{Mg_5Si_6}} - \mathbf{U}_{\mathrm{Al}}\mathbf{S}||_{\mathrm{F}}$. We determine this matrix by finding the matrix $\mathbf{Q}$ solving

$$\mathbf{U}_{\mathrm{Mg_5Si_6}} = \mathbf{U}_{\mathrm{Al}} \cdot \mathbf{Q},$$

and then rounding each element of $\mathbf{Q}$ to the nearest integer to define $\mathbf{S}$. This results in the integer matrix

$$\mathbf{S} = \begin{bmatrix} 3 & -2 & 0 \\ 2 & 1 & 0 \\ 0 & 0 & 1 \end{bmatrix},$$

and it may be checked that by increasing or decreasing any of the elements by 1, the norm increases. By using $\mathbf{U}_{\mathrm{Mg_5Si_6}}$ and $\mathbf{U}^*_{\mathrm{Al}} = \mathbf{U}_{\mathrm{Al}}\mathbf{S}$ in Eq. 3.16, the transformation matrix becomes

$$\mathbf{P} = \begin{bmatrix} 0.919 & 0.203 & 0 \\ 0.146 & 0.836 & 0 \\ 0 & 0 & 0.994 \end{bmatrix}.$$

Inserting this matrix into Eq. 3.17 obtains the misfit strain tensor

$$\epsilon^0_{ij}(c) = \frac{c + c_{\mathrm{eq}}}{2c_{\mathrm{eq}}} \begin{bmatrix} -0.0672 & 0.1542 & 0 \\ 0.1542 & -0.1299 & 0 \\ 0 & 0 & -0.0059 \end{bmatrix}.$$

Chapter 4

Computational method

The phase-field calculations in this thesis were performed using the Multiphysics Object-Oriented Simulation Environment (MOOSE) framework. This framework is built using the finite element method (FEM) for solving partial differential equations (PDEs), which we briefly introduce in order to look at how the convergence of the calculations is defined using residuals. MOOSE contains implementations of residuals many PDEs, as well as functionality connected to setting up simulations and post-processing the results. It also contains a probabilistic nucleation model, which we implement into our phase-field calculations.

4.1 The MOOSE framework

MOOSE is an open-source framework that was developed at the Idaho National Laboratory (INL) [16, 51], and contains modules for several different fields of physics. In our thesis, the phase-field, heat conduction and tensor mechanics modules are used to implement our phase-field model. The framework is built using the finite element method, which will be introduced in the next section, and is capable of running simulations using parallelisation. It also allows for multi-scale modelling through the use of multi-apps, where information can be transferred between the different simulations/apps. We use this capability to run several similar simulations of our systems in the nucleation region and calculate the average fraction of precipitated area across these simulations, in order to minimise the influence on the results by the randomness connected to the probability of nucleation.

The framework is written in C++, and users have the possibility of writing their own custom applications. Meanwhile, the input files for the simulations are built using a syntax based on blocks and sub-blocks. Each block defines an important part of the simulation setup, such as the mesh, the boundary and initial conditions, the parameters and functions used in the equations, the solver etc. As an example, we look at the implementation of the mesh in our simulation. We choose to discretise our $100 \times 100\,\mathrm{nm}^2$ system into a uniform quadratic mesh of 200×200 points, which is implemented into the simulation through the block

```
[Mesh]
  type = GeneratedMesh
  dim = 2
  elem_type = QUAD4
  nx = 100
  ny = 100
  xmin = 0
  xmax = 100
  ymin = 0
  ymax = 100
  uniform_refine = 1
[]
```

Here, we have used the command `uniform_refine = 1` because we apply adaptive mesh refinement and coarsening on the grid in the executioner block. By using an adaptive mesh, the mesh can be refined in regions of high error while coarsening regions of low error, which in turn can lead to a lower computational cost of the simulations. In our system, we expect to need a fine grid at the phase boundaries between the matrix and the precipitates, while the regions located in either the matrix or the bulk of the precipitates are expected to have lower error, justifying the usage of a coarser mesh in these regions. We choose to refine an element of the mesh if the error of that element divided by the max error across the system is higher than 0.8, and the refinement is performed by splitting the element into four quadratic elements. Meanwhile, we choose to coarsen the mesh if the average fraction of error in four neighbouring elements is smaller than 0.05, causing the four elements to combine into a single quadratic element. However, we only allow the system to refine and coarsen the mesh one level from the initial mesh. We also use an adaptive time step, which increases or decreases the current time step, depending on how many iterations of calculations are performed before the solution achieves convergence within our convergence criteria.

In addition to finding the evolution of the phase-field variables, we can also extract other results from the simulations using the postprocessing block. We obtain the total free energy of the system by integrating the total free energy density across the mesh, which can be uses to show that the temporal evolution moves the system towards thermodynamic equilibrium. We can also find the fraction of precipitate area by defining a function

$$p\left(\mathbf{r}\right) = \begin{cases} \dfrac{1}{A} & , \, c\left(\mathbf{r}\right) > c_{\text{eq}} - 0.1 \\ \\ 0 & , \, \text{otherwise} \end{cases} ,$$

where $A = 1 \times 10^4\,\text{nm}^2$ is the area of the system. The fraction of area associated with the precipitates in the system is then found by integrating this function over the mesh.

An example input file for a phase-field simulation with elastic strain effects on an initial rectangular-shaped precipitate can be seen in Appendix A. A more detailed introduction to the syntax and applications of the MOOSE framework can be found in the thesis of Tyler S. Trogden [52] or by studying the documentation and tutorials at https://mooseframework.inl.gov/index.html.

4.2 The finite element method

The finite element method (FEM) is a method for partial solving differential equations numerically. Similar to the finite difference method, the domain of our system is discretised into a mesh of points

$$(x,\ y)_{ij} = \left(i\frac{L_x}{N_x},\ j\frac{L_y}{N_y}\right),$$

where L_x and L_y are the lengths of the system (in our case $L_x = L_y = 100\,\text{nm}$)

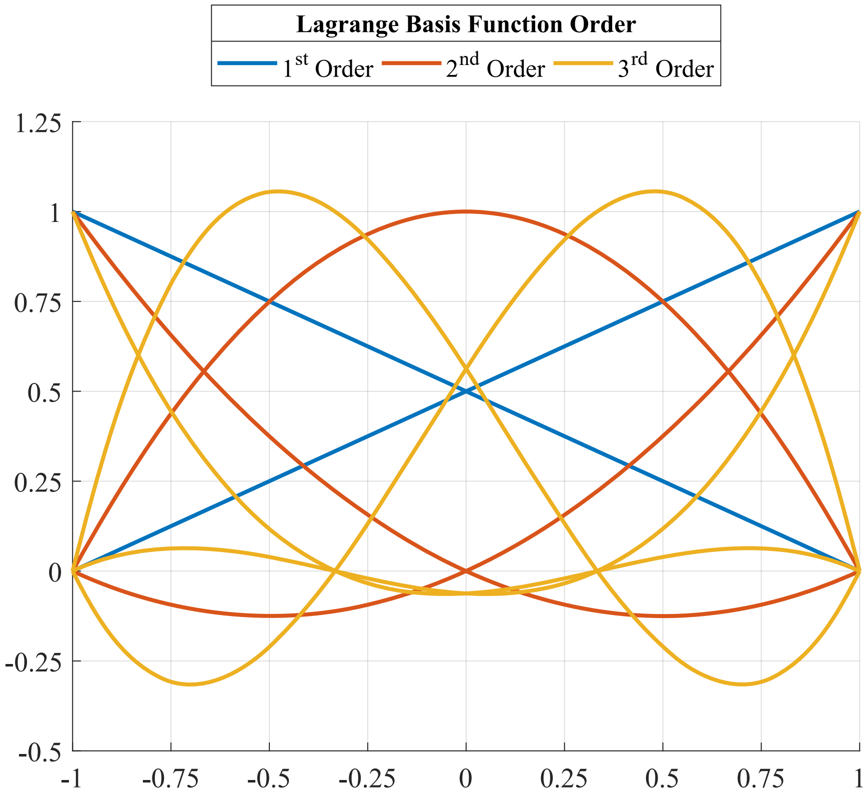

Figure 4.1. *The first, second and third order Lagrange basis functions in 1D. Here, the points* -1 *and* 1 *correspond to discretised points in the mesh. Figure by Ferentzfever, distributed under a CC0 1.0 licence (https://en.wikipedia.org/wiki/File:Lagrange_basis_functions.svg#filelinks).*

and N_x and N_y are the number of discretised points in the x- and y-direction, respectively. However, the difference between these two methods is that the finite element method calculates a continuous solution for the entire domain, while the finite difference method only calculates the solution at the discretised points. The solution in the finite element method is given by a linear combination of a set of basis functions, where each basis function is characterised by being equal to 1 at only one of the discretised points while being 0 in all the other discretised points. There exist many sets of basis functions to choose from, classified by family and order of the basis functions. In this thesis, we choose to use a set of first order Lagrange basis functions $\{\phi_i\}$, which are linear functions as shown in Fig. 4.1.

The Cahn-Hilliard equation in Eq. 3.9 is a fourth-order differential equation, but it can be split into two second-order differential equations by using the chemical potential μ in Eq. 3.6, giving

$$\frac{\partial c}{\partial t} = \nabla M \nabla \mu,$$
$$\mu = \frac{\partial f_{\text{loc}}}{\partial c} - \kappa \nabla^2 c.$$

In order to solve these two equations using the FEM, we need to express them in weak form, which is found by multiplying both sides of the equations by a test function ψ and integrating over the entire domain, giving

$$\int_{\Omega} \psi \frac{\partial c}{\partial t} \, \mathrm{d}V - \int_{\partial\Omega} \psi \left(M \nabla \mu \cdot \hat{n} \right) \, \mathrm{d}s + \int_{\Omega} \nabla \psi \cdot \left(M \nabla \mu \right) \, \mathrm{d}V = 0,$$

$$\int_{\Omega} \psi \mu \, \mathrm{d}V - \int_{\Omega} \psi \frac{\partial f_{\text{loc}}}{\partial c} \, \mathrm{d}V + \int_{\partial\Omega} \kappa \psi \left(\nabla c \cdot \hat{n} \right) \, \mathrm{d}s - \int_{\Omega} \kappa \nabla \psi \cdot \nabla c \, \mathrm{d}V = 0.$$

By expressing μ and c as linear combinations of the basis functions

$$\mu \left(\mathbf{r} \right) \approx \mu_h = \sum_i \mu_i \phi_i \left(\mathbf{r} \right) \ , \quad c \left(\mathbf{r} \right) \approx c_h = \sum_i c_i \phi_i \left(\mathbf{r} \right),$$

and by using the same basis functions as test functions $\psi = \{\phi_i\}_{i=1}^{N}$, the i^{th} components of the residual vectors are given by

$$R_i \left(\mu_h \right) = \int_{\Omega} \psi_i \frac{\partial c_h}{\partial t} \, \mathrm{d}V - \int_{\partial\Omega} \psi_i \left(M \nabla \mu_h \cdot \hat{n} \right) \, \mathrm{d}s + \int_{\Omega} \nabla \psi_i \cdot \left(M \nabla \mu_h \right) \, \mathrm{d}V,$$

$$R_i \left(c_h \right) = \int_{\Omega} \psi_i \mu_h \, \mathrm{d}V - \int_{\Omega} \psi_i \frac{\partial f_{\text{loc}}}{\partial c_h} \, \mathrm{d}V + \int_{\partial\Omega} \kappa \psi_i \left(\nabla c_h \cdot \hat{n} \right) \, \mathrm{d}s - \int_{\Omega} \kappa \nabla \psi_i \cdot \nabla c_h \, \mathrm{d}V$$

where the integrals can be approximated using Gaussian quadrature. There exist several methods for solving these residual equations, but we choose to use Newton's method because we found that this method converges faster for our system than methods such as the Preconditioned Jacobian Free Newton Krylov (PJFNK) method. The downside of using Newton's method is that this method needs to calculate the full and accurate Jacobian of the system, while the PJFNK method does not need the Jacobian to be as accurate, and it may neglect the off-diagonal terms. We use the implicit Euler method as the time-integrator in our calculations.

These residuals express the error of the approximated solutions μ_h and c_h on the discretised mesh, and these values are used to determine when to accept a solution. The residuals of the equations connected to elastic strain and electric field contributions are calculated in a similar fashion. In our simulations, we use the convergence criteria of $|\mathbf{R}| < 1 \times 10^{-7}$.

In MOOSE, the equations and residual calculations are easily implemented into the simulations using the `Kernels` block, and the physics modules in MOOSE have many kernels containing residuals for different PDEs. For our case of the split Cahn-Hilliard equation, we utilise the kernels `CoupledTimeDerivative`, `SplitCHWRes` and `SplitCHParsed`, and all we need to write in our input file to implement these kernels into the system is

```
[Kernels]
  [c_dot]
    type = CoupledTimeDerivative
    variable = w
    v = c
  []
  [coupled_res]
    type = SplitCHWRes
    variable = w
    mob_name = M
  []
  [coupled_parsed]
    type = SplitCHParsed
    variable = c
    f_name = f_loc
    kappa_name = kappa_c
    w = w
  []
[]
```

4.3 Nucleation model

The phase-field module in MOOSE contains two different methods for implementing nucleation into a simulation. The first method adds a random noise term $\eta\left(t, \mathbf{r}\right)$ to the Cahn-Hilliard equation, causing random nucleation during the microstructure evolution. The second method is referred to as discrete nucleation, and this is the method we use to model nucleation in our simulations.

The discrete nucleation system in MOOSE triggers the formation of nucleation events artificially by changing the value of an order parameter (c in our case) in a sphere around the points of nucleation, while simultaneously modifying the free energy density locally around the nuclei by adding a penalty energy term. The insertion of a nucleation event at time t into the system is governed by a probability function of the form

$$P\left(t, \mathbf{r}\right) = 1 - \exp\left(-J\Delta t\right),$$

where Δt is the time step in the simulation and J is the local nucleation rate. We assume a homogeneous nucleation rate, and classical nucleation theory expresses the local nucleation rate for homogeneous nucleation as [53]

$$J = \rho Z j \exp\left(-\Delta F^{*}/kT\right),$$

where ρ is the number density of molecules, Z is the Zeldovich factor, which gives the probability of a nucleus at the top of the nucleation barrier forming a precipitate, j is the rate of molecules attaching to the nucleus, and ΔF^{*} is the activation energy needed to form a nucleus at the top of the nucleation barrier. This nucleation barrier is found by looking at the radius-dependence of the sum of the volumetric bulk free energy and the surface energy for a precipitate. However, due to difficulty in determining the values of these quantities, we decide to set the nucleation rate to $J = 5 \times 10^{-7}$, as this value gives a good representation of the nucleation mechanisms we wish to study.

The order parameter c in our phase-field model is conserved, and it is therefore important to make sure that the insertion of nucleation events upholds the conservation of this phase-field variable throughout the simulation. The implementation of the discrete nucleation system in MOOSE accounts for this by lowering the value of c around the nucleation events. Additionally, we hold the inserted nucleation events at the target value of the order parameter for 360 seconds, in order to let solutes diffuse towards the nucleation event so that the nuclei may stabilise. As mentioned, the local free energy density is also modified near the nucleation sites in order to make the precipitates into lower energy states, increasing the diffusion of solutes towards the precipitates. After the hold-time of a nucleation event, the nucleation energy term associated with that event is removed.

We choose to study nucleation events of radius 1 nm and 2 nm to see if the size of the initial nucleation events impacts the evolution of the system. The target value of the events is set to $c = c_{\mathrm{eq}}$, and we make the nuclei have a smooth interface of width equal to the radius of the events in an effort to help the simulations converge faster.

Chapter 5

Results and discussion

We now present and discuss the results from our phase-field simulations. First, we study how the simulations are affected by allowing the temperature to vary in our system of dimensions $100 \times 100\,\mathrm{nm}^2$, and then we simulate the isothermal evolution of the composition field, where we study the phase separation for different initial conditions of the composition phase-field variable. Simulation results of the interface profile between the aluminium matrix and the precipitates, the minimisation of the total free energy and the evolution of the area fraction occupied by precipitates are also presented and discussed. For the nucleation-driven system, we look at the averaged graph of the fraction of precipitate area from 10 simulations of the same system, where the random seeds were changed, in order to decrease the dependence on the random number generators used in the simulations.

We also study the precipitation process when a DC electric field is applied across the system with a potential drop of $\Delta V = 1 \times 10^{-2}\,\mathrm{V}$. Here, we discuss the effects of the electron wind force in our phase-field model and compare these to the results from experimental studies of this ageing process. Finally, we consider phase-field simulations with contributions from the elastic strain on the precipitates due to the lattice misfit between the precipitates and the aluminium matrix. We look at initial conditions for c containing initial precipitates shaped like squares and rectangles to study the evolution of the shapes of the precipitates due to initial displacements and minimisation of the total free energy.

5.1 Temperature fluctuations

In the beginning of this thesis work, we thought it would be interesting to allow temperature fluctuations in our system, as the process of forming precipitates is expected to release heat at the phase boundaries. We started out by considering the evolution of the temperature without heat sources, and looked strictly at the temperature evolution driven by diffusion. We modelled this using the simple diffusion equation in Eq. 3.11 with the initial and boundary conditions defined in Section 3.3, but we noticed that the temperature distributed itself evenly across the system during the first time step $\Delta t = 1\,\mathrm{s}$, which indicated that the diffusive behaviour of the temperature field made the temperature quickly reach an equilibrium state. We therefore decided to calculate a characteristic time scale using the Buckingham π-theorem, which states that any equation of n variables can be rewritten in terms of $p = n - k$ dimensionless variables (π-groups), where k is the number of physical dimensions involved in the equation [54].

The temperature field can be expressed as the function $T\left(t, x, y, D_T\right)$, and the units of the dependencies in this function are

$$[t] = \mathrm{s}, \quad [x] = \mathrm{m}, \quad [y] = \mathrm{m}, \quad [D_T] = \mathrm{m}^2/\mathrm{s}.$$

From this, we get that the T-function is dependent on 4 variables, while there are only two physical dimensions in the system (metres and seconds), which means that the problem can be rewritten in terms of $p = 4 - 2 = 2$ π-groups.

We choose to make the two π-groups proportional to x and y, respectively, and thus express them as $\pi_x = x t^a D_T^b$ and $\pi_y = y t^c D_T^d$. Since these two groups need to be dimensionless, the parameters a, b, c and d are chosen so that this criterion is fulfilled. We can easily find that $a = b = c = d = -1/2$ makes the two π-groups dimensionless, giving

$$\pi_x = \frac{x}{\sqrt{D_T t}}\ , \quad \pi_y = \frac{y}{\sqrt{D_T t}}.$$

This lets us express the temperature as $T\left(\pi_x, \pi_y\right)$, and if we now consider the temperature in an arbitrary point, e.g. $(1, 3)$, we know that $T\left(1, 3\right)$ must be constant regardless of changes in x, y and t. From this we can see that the expressions $x = \sqrt{D_T t}$ and $y = 3\sqrt{D_T t}$ must be upheld in this point, showing that a point of constant temperature propagates in x and y proportional to $\sqrt{D_T t}$. Our system is of dimensions $100 \times 100\,\mathrm{nm}^2$, so in order to find a characteristic time scale for the temperature, we consider the time it takes for a temperature front to propagate 100 nm. By rewriting the proportionality relation between x and t, we get

$$t = \frac{x^2}{D_T} = \frac{100\,\mathrm{nm}^2}{6.4 \times 10^{13}\,\mathrm{nm}^2/\mathrm{s}} = 156\,\mathrm{ps}.$$

We notice that the time scale for the propagation of the temperature is several orders of magnitude smaller than the time steps used in our simulations, which gives an explanation of why the temperature reached equilibrium within a single time step. We also note that because the temperature diffuses so quickly, we do not expect fluctuations in temperature caused by the formation of precipitates to impact the system. In addition, we assume that the temperature of the macroscopic sample of the alloy is held at a constant temperature, and thus the heating of the macroscopic sample from the precipitation process is disregarded in our system.

To check that our characteristic time scale calculation was correct, we simulate the temperature evolution with the initial condition in Fig. 3.6 with time steps in the order of picoseconds. We can see from Fig. 5.1 that the temperature field is approximately evenly distributed across the system after 40 ps, as expected from our time scale calculation and the shape of the temperature initial condition. Considering our discoveries in this section, we disregard fluctuations in the temperature of our simulations, and instead consider systems at constant temperature $T = 450\,\mathrm{K}$.

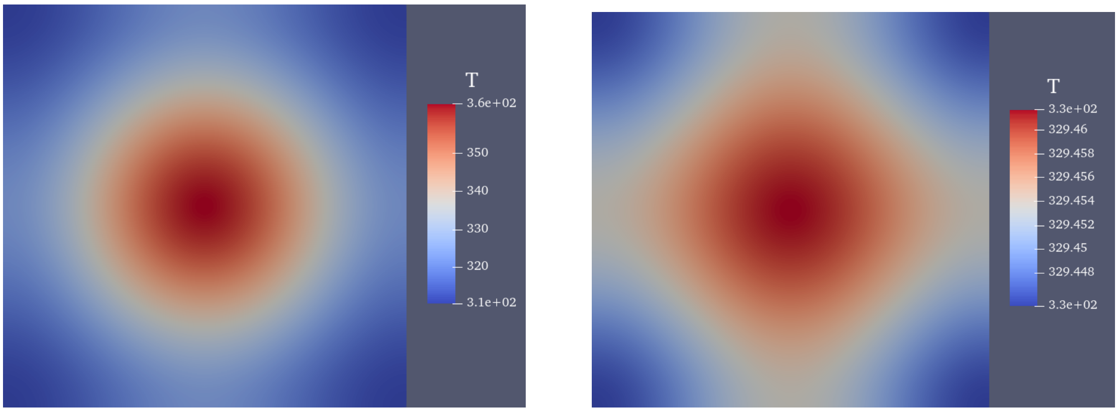

(a) **(b)**

Figure 5.1. ***(a)*** *Temperature field at* $t = 5\,\mathrm{ps}$. ***(b)*** *Temperature field at* $t = 40\,\mathrm{ps}$.

5.2 Comparison of the precipitation in different systems

5.2.1 Testing our model and the implementation

We begin by looking at simulations of our phase-field model without contributions from any additional fields, and want to check that both the model and the implementation into MOOSE lead to simulations with the expected characteristics. Therefore, we start by considering the system in the spinodal region, given by the random distribution of c in the interval $[-0.12, -0.08]$ as shown in Fig. 5.2.

The temporal evolution of c, calculated using Eq. 3.9, is shown in Fig. 5.3, where we can see that the system has spontaneously separated into two phases at $t = 1\,\mathrm{h}$. We note that $c \approx \pm c_{\mathrm{eq}}$ in the bulk of the phases, which is what we expect for the spinodal case. We also observe that the precipitates coarsen for increasing time t due to Ostwald ripening as expected, leading to fewer and larger precipitates at $t = 24\,\mathrm{h}$ with respect to the system at $t = 1\,\mathrm{h}$. If we had increased the simulation time, it is natural to expect that we would eventually end up with a single precipitate in the system. This mechanism was expected as the coalescing of precipitates lowers the total interface energy of the system. This can be confirmed by looking at the evolution of the total free energy of the system in Fig. 5.4, which is seen to be decreasing towards an equilibrium state.

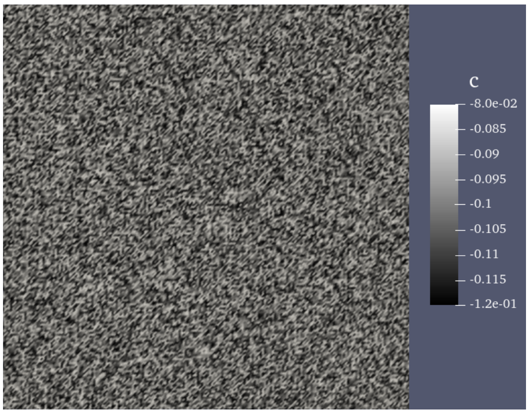

Figure 5.2. *Initial condition of c given by random distribution in the interval* $[-0.12, -0.08]$*, which is expected to lead to spinodal decomposition.*

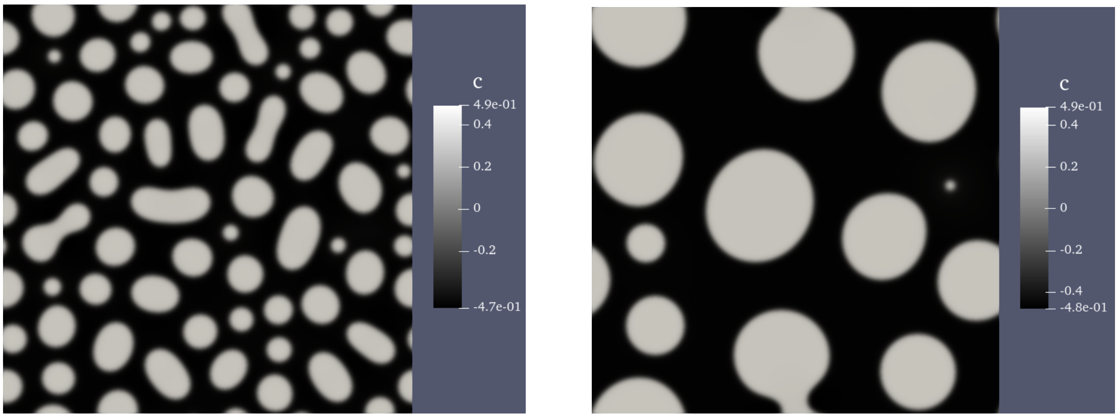

(a) $t = 1\,\mathrm{h}$ **(b)** $t = 24\,\mathrm{h}$

Figure 5.3. *Simulation results of the system without additional field contributions defined in the spinodal region.*

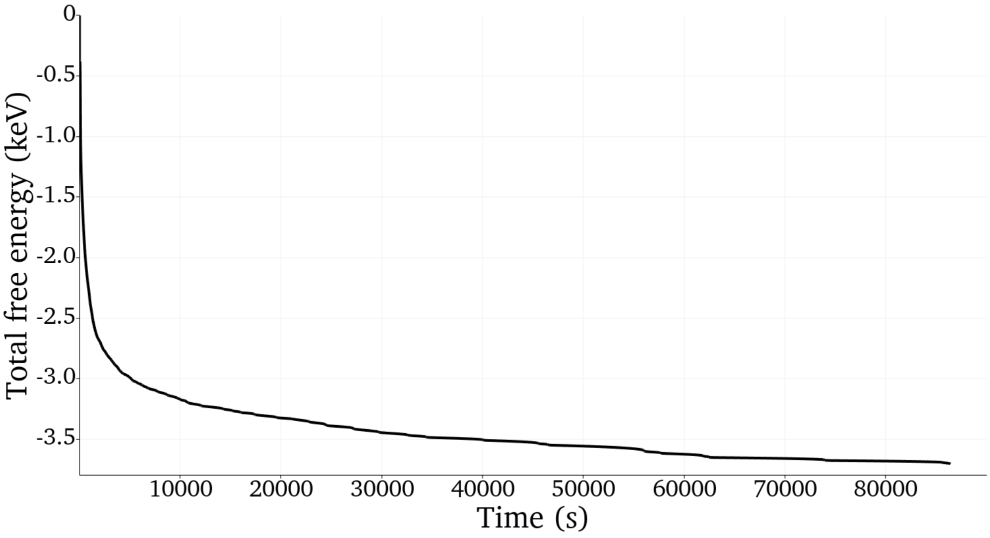

Figure 5.4. *Temporal evolution of the total free energy of the system in the spinodal region.*

The phase boundaries between the precipitates and the matrix are found to be sufficiently sharp, as we observe the existence of very small precipitates at $t = 1\,\mathrm{h}$. If the phase boundaries were too diffuse, the initial precipitates would be significantly coarser, as the diffuse phase boundaries would lead to faster coalescing of the smaller precipitates. By plotting the value of c over a line across a phase boundary, as shown in Fig. 5.5, we find that the phase boundary has a width of approximately $2\,\mathrm{nm}$, which is the value we used when choosing the value of κ in Section 3.3.

We apply adaptive mesh refinement on the mesh in order to minimise the computational cost of the simulations without decreasing their accuracy. Fig. 5.6 shows the mesh of the spinodal system at $t = 24\,\mathrm{h}$, where the mesh is seen to be significantly finer at the phase boundaries than in the bulk of the phases. This is as expected since the gradients of the functions in our model are greater in these regions.

We are also interested in the evolution of the fraction of precipitated area, as this property is related to the hardness of the alloys. In Fig. 5.7 we see that the fraction of precipitated area has a similar curve to the hardness curves reported in previous experimental studies [9], except that the values do not decrease after

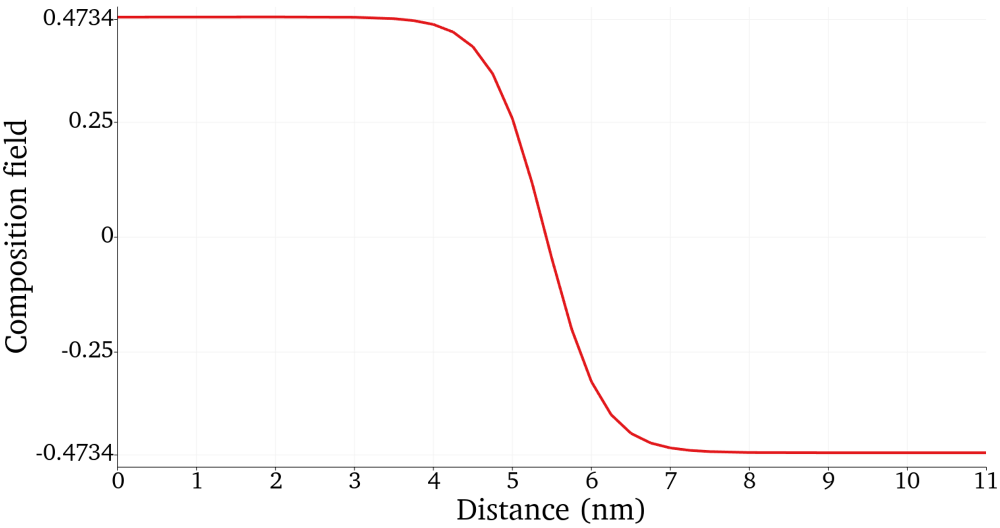

Figure 5.5. *Plot of c along a line across the phase boundary between a precipitate and the matrix. The interface profile has a thickness of approximately* $2\,\mathrm{nm}$.

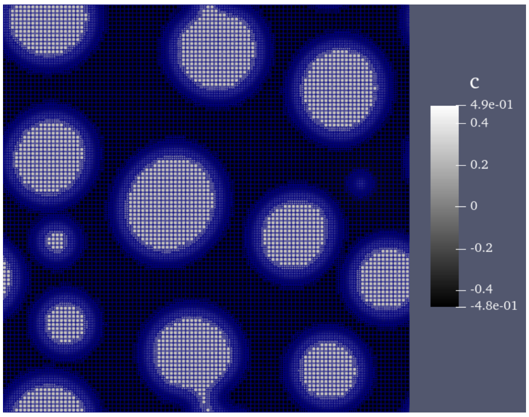

Figure 5.6. *Mesh adaptivity for the spinodal system at* $t = 24\,\mathrm{h}$*, where the mesh is refined at the phase boundaries, while coarsened in the bulk of the individual phases.*

reaching a peak value. This is because our model does not take into account that the precipitates restructure into more stable precipitates that give lower hardness to the alloy than the β'' precipitates. These results indicate that our phase-field model and the implementation in MOOSE behave as expected.

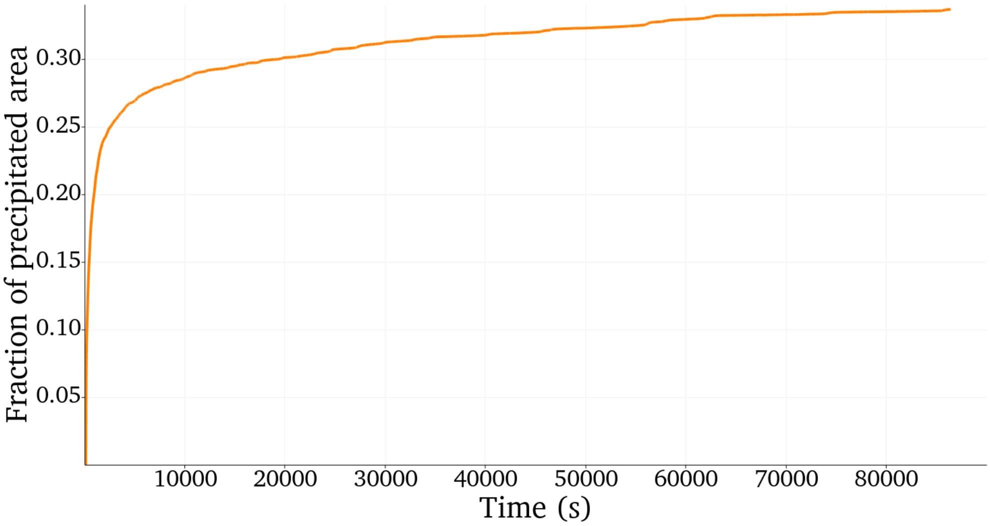

Figure 5.7. *Evolution of the area fraction of precipitates in the spinodal system.*

5.2.2 Nucleation-dependent simulations

Since the model behaves as expected, we proceed by looking at the system in the nucleation region of the phase diagram, given by the initial condition shown in Fig. 3.4. We perform two different simulations, one with nucleation events with radii of 1 nm and one with radii of 2 nm in order to study whether the size of the initial events impacts the coarsening of the precipitates. By comparing the composition fields in Fig. 5.8 and Fig. 5.9, we do not notice major differences in the precipitation.

The smallest precipitates seen in the plots at $t = 1\,\mathrm{h}$ are the inserted nucleation events, while the larger precipitates are previously inserted nucleation events that have attracted solutes to their phase boundary, and thus increased their size. The larger precipitates at $t = 24\,\mathrm{h}$ are seen to be of approximately the same size, independent of the radius of the initial nucleation events, indicating that the size of the initial nuclei have little importance in the coarsening of the precipitate.

We note from Fig. 5.10 that the insertion of nucleation events causes fluctuations in the fraction of precipitated area when the system is close to an equilibrium state. This is because the composition field at the nucleation events is held at c_{eq} for the hold-time of 360 s, even though the system cannot sustain the formation of more precipitates. As a result, we prefer simulating the system with smaller initial nucleation events, as their lower area give smaller fluctuations in the fraction of

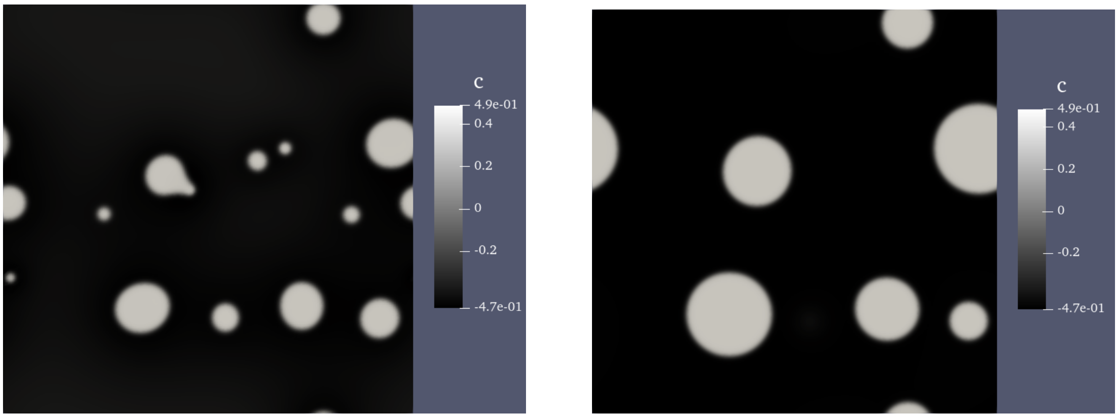

(a) $t = 1\,\mathrm{h}$ **(b)** $t = 24\,\mathrm{h}$

Figure 5.8. *Simulation results of the nucleation system, driven by chemical diffusion and insertion of nucleation events with radii of* 1 nm.

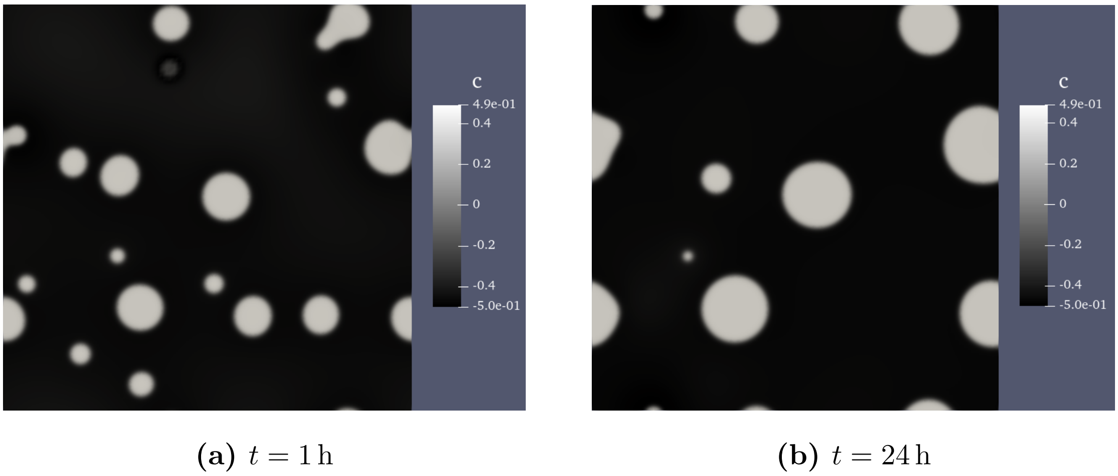

(a) $t = 1\,\mathrm{h}$ **(b)** $t = 24\,\mathrm{h}$

Figure 5.9. *Simulation results of the nucleation system, driven by chemical diffusion and insertion of nucleation events with radii of* $2\,\mathrm{nm}$.

precipitated area. This is also reflected in Fig. 5.10, where the fluctuations are seen to be larger for the system with nucleation events of radii $2\,\mathrm{nm}$.

This fluctuation issue is also the reason for not choosing a higher nucleation rate in our simulations. A method to potentially remove this problem would be to stop inserting new nucleation events after a chosen time $t_{\mathrm{cut-off}}$, and then let the system evolve strictly due to the chemical diffusion of the Cahn-Hilliard equation. However, the discrete nucleation system in MOOSE does not offer this

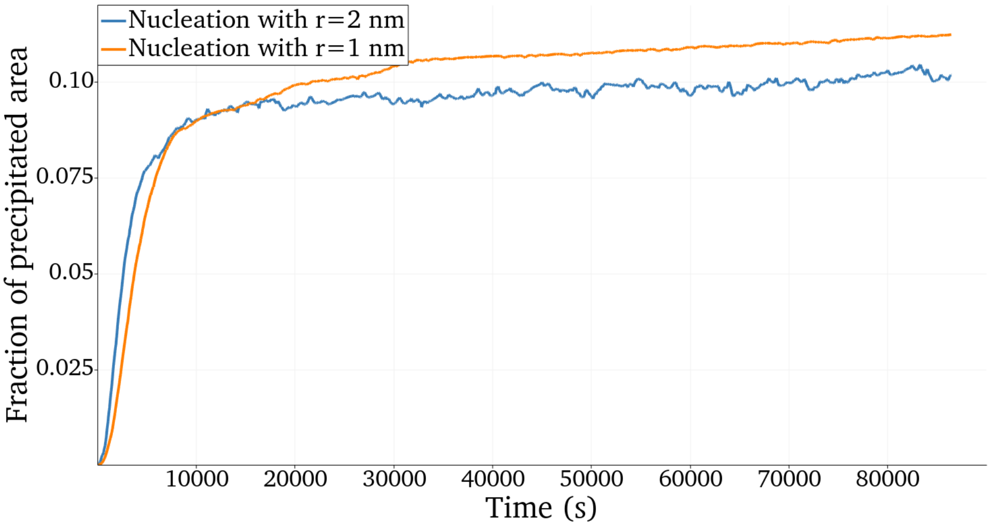

Figure 5.10. *Evolution of the area fraction of precipitates for the nucleation systems with initial nucleation events of radii* $1\,\mathrm{nm}$ *and* $2\,\mathrm{nm}$.

functionality of specifying a cut-off time for the nucleation, and we would therefore have to write this functionality into the framework ourselves.

5.2.3 MultiApp simulations

In an attempt to minimise the fluctuations of the fraction of precipitated area caused by the probabilistic nucleation model, we use the MultiApp functionality in MOOSE to run 10 almost similar simulations of each system. The only difference between them is that we change the random seeds for the random number generators used to determine the initial condition of c and when a nucleation event should be inserted. The effect of the randomness associated with the nucleation probability is expected to be more significant for the results than the randomness in the initial condition. By averaging the data for the fraction of precipitated area in these 10 simulations, it makes the results less dependent on the randomness of our model. By comparing the plots of the fraction of precipitate area in Fig. 5.10 against the plots of the averaged values in Fig. 5.11, we notice that the averaged values give smoother graphs than the values from the individual simulations, especially for the system of initial nucleation events with radii 2 nm. Thus, we note

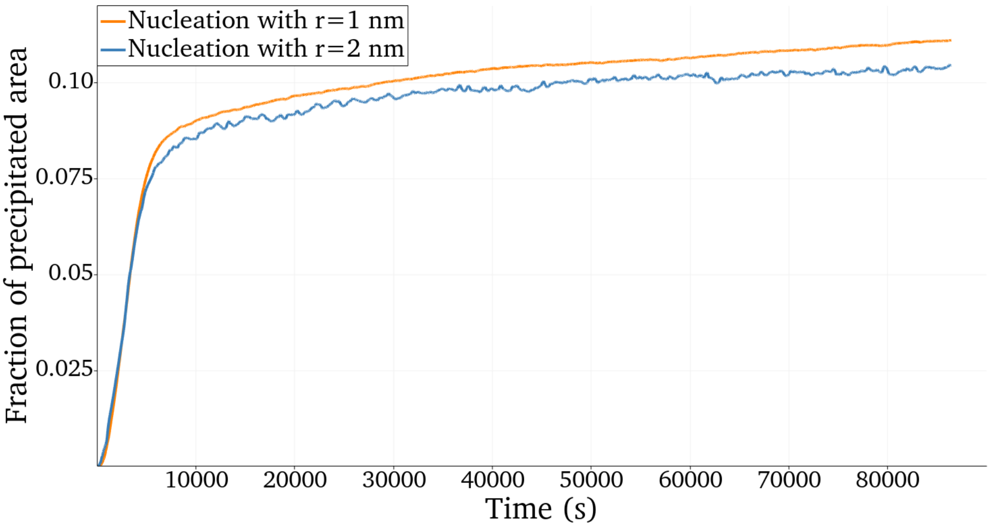

Figure 5.11. *Area fraction of precipitates for the nucleation systems with initial nucleation events of radii* 1 nm *and* 2 nm*, averaged from* 10 *simulations with different random seeds.*

that if the results from a phase-field model with a probabilistic nucleation model such as our model is to be used for quantitative calculations, it may be beneficial to make the production runs by performing several similar simulations, and then sample the average data from these simulations.

5.2.4 Simulations with applied DC electric field

When applying a DC electric field across the system, we need to solve Eqs. 3.12 and 3.13 in our simulation, where we choose to use the potential drop $V_0 = 1 \times 10^{-2}\,\mathrm{V}$ across our system in the x-direction. We decide to only consider the systems with initial nucleation events with radii 1 nm now. In Fig. 5.12 we see the evolution of the composition field in the applied DC electric field, and we immediately notice that the precipitates are diffusing towards the right side of the system. This evolution can be explained by the effective force on the precipitates from the electron wind. By simulating our system in the spinodal region with the same electric field, we see a similar evolution in Fig. 5.13.

By subtracting the average electric field, $\mathbf{E}_0 = -\nabla V = (-1 \times 10^{-4}\,\mathrm{V/nm})\ \hat{x}$, from the total electric field across the system in our simulation, we can see from Fig. 5.15 that the electric field around the circular precipitates bends towards the

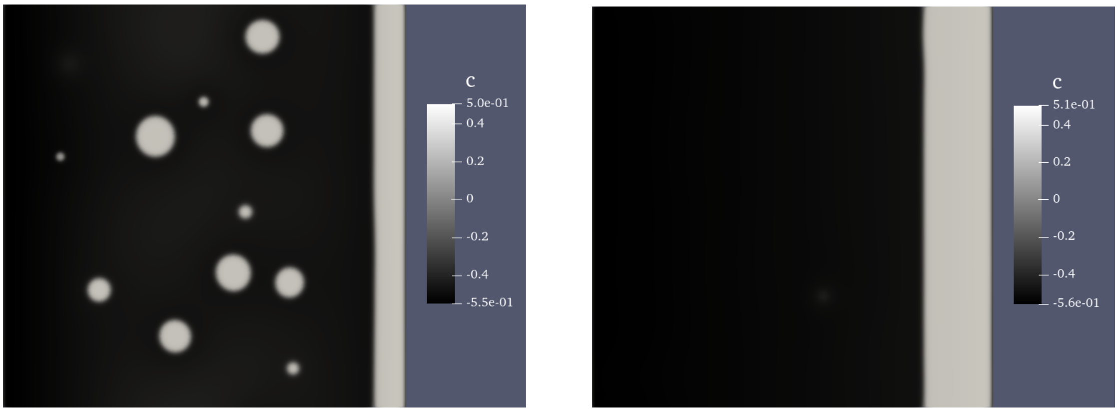

(a) $t = 1\,\mathrm{h}$ **(b)** $t = 24\,\mathrm{h}$

Figure 5.12. *Simulation results of the nucleation system with an applied DC electric field, given by a potential drop* $\Delta V = 1 \times 10^{-2}\,\mathrm{V}$ *across the system. The evolution of* c *is driven by chemical diffusion, electromigration and insertion of nucleation events with radii of* $1\,\mathrm{nm}$.

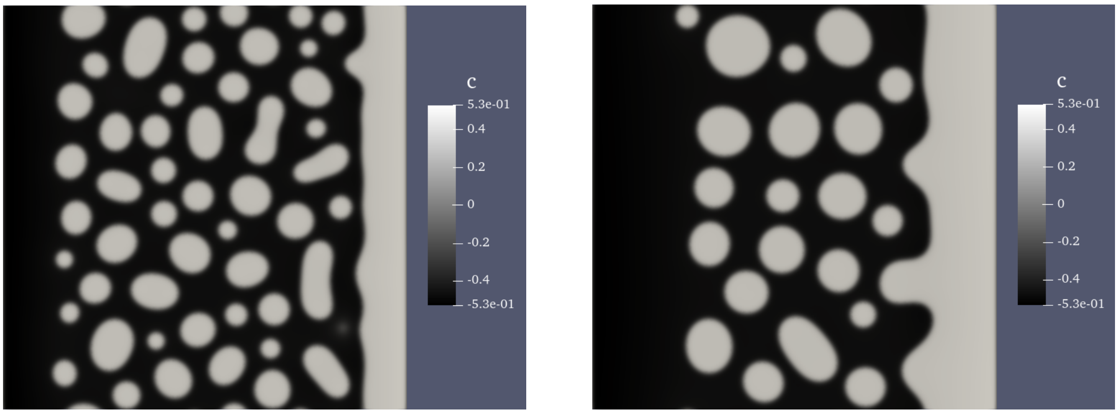

(a) $t = 1\,\mathrm{h}$ **(b)** $t = 3\,\mathrm{h}$

Figure 5.13. *Simulation results of the spinodal system with an applied DC electric field, given by a potential drop* $\Delta V = 1 \times 10^{-2}\,\mathrm{V}$ *across the system, causing the evolution of* c *to be driven by chemical diffusion and electromigration.*

precipitates. This indicates that the diffusion of the solutes in the matrix with respect to the precipitates is affected by the applied electric field, but the strength of this field is seen to be significantly weaker than the electric field that attracts the precipitates towards the right side of the system.

This evolution mechanism of c is found to be similar to the evolution reported by Liang et al. [34], where the precipitate phase migrated towards one side of the sample. Naturally, this leads to faster coarsening of the precipitates, which is also seen by comparing the plots of the fraction of precipitated area for the different systems in Fig. 5.14. However, this behaviour is not found in the microstructure images and explanations presented in the previous experimental studies that were mentioned in Section 2.2. This may indicate that the electron wind has a smaller impact on the precipitation process in real aluminium alloys than in our model. We note that the β'' precipitates are semi-coherent structures, and are often considered to be immobile in the microstructure. The electron wind force is given by the exchange of momentum from electrons onto the metal ions in the lattice, and the coherency of the precipitates in the structure might therefore be the reason for the low impact from the electron wind on the microstructure of real alloy samples. Meanwhile, the phase-field model allows the precipitates to move around in the system. This presents a significant difference between the evolution in the

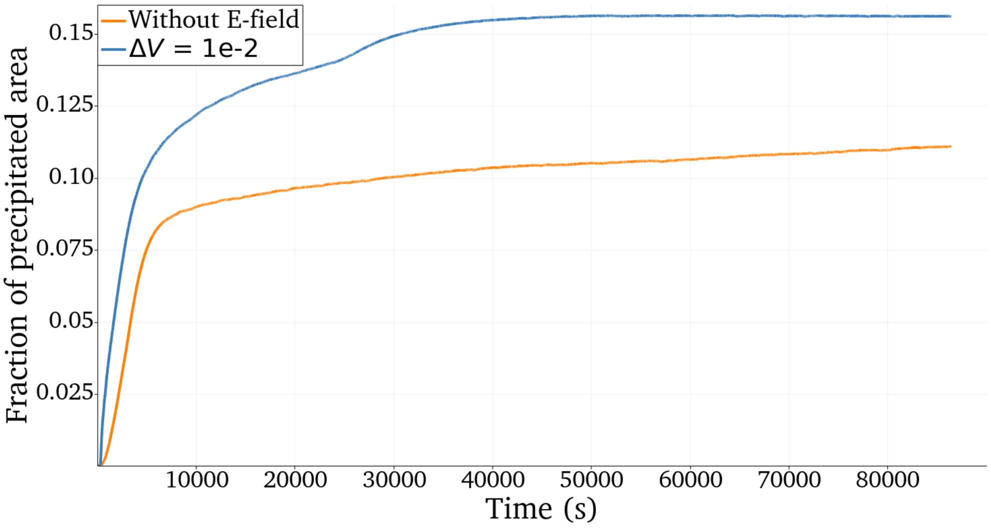

Figure 5.14. *Area fraction of precipitates for the nucleation systems with and without an applied DC electric field.*

phase-field model and precipitate formation mechanisms in real alloys, where the evolution of precipitates in real alloys is driven by the diffusion of solute atoms that merge into the precipitate structures when they reach the phase boundaries.

It might therefore be of interest in future work to look into how the diffusion process of the solute atoms is affected by an applied DC electric field without modelling an effective force on the precipitates. One effect that might increase the diffusion rate of the solute atoms is the electric field related to the formation of

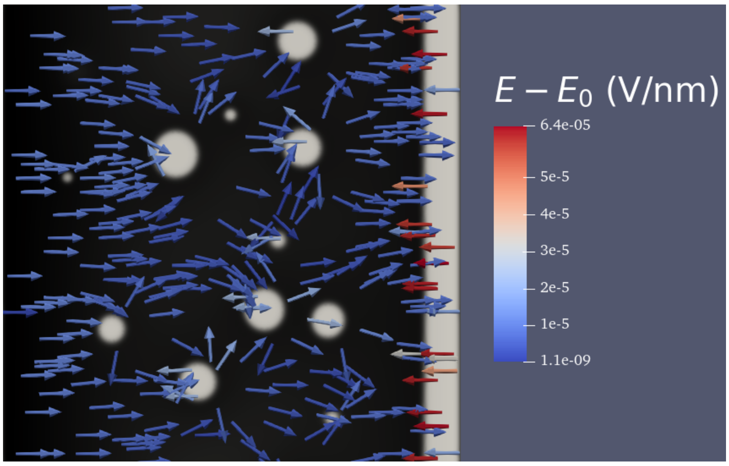

Figure 5.15. *The difference between the total electric field and the average electric field,* $\mathbf{E} - (-1 \times 10^{-4}\,\mathrm{V/nm})\ \hat{x}$*, for the nucleation systems at* $t = 1\,\mathrm{h}$*.*

an electric dipole moment across a precipitate due to the applied electric field, as this could present an attractive force onto the solute atoms in the matrix.

5.3 Simulations with misfit strain effects

When implementing the elastic strain field contributions into the simulations, the solver encountered problems with converging towards a solution. We found that by applying the PJFNK method with the two-step backward differentiation formula (BDF2) as the time integrator instead of Newton's method with the implicit Euler method, the solver was able to achieve convergence within our chosen convergence criteria. We do however note that this change of solver led to significantly higher computational costs for the simulations.

To study the preferred shape of the β'' precipitates, we begin by simulating the evolution of a square-shaped precipitate of dimensions $20 \times 20\,\mathrm{nm}^2$, as shown in Fig. 3.5a. The resulting evolution is presented in Fig. 5.16, where we can see that the initial misfit strain stretches the precipitate along the diagonal. The precipitate then proceeds by stretching even further in this direction, while being compressed along the other diagonal, until it reaches a stabilised shape that looks like a needle. Thus, our phase-field simulation is able to recreate the same shape of the β'' precipitate as the shape found in the microstructure of Al−Mg−Si alloys,

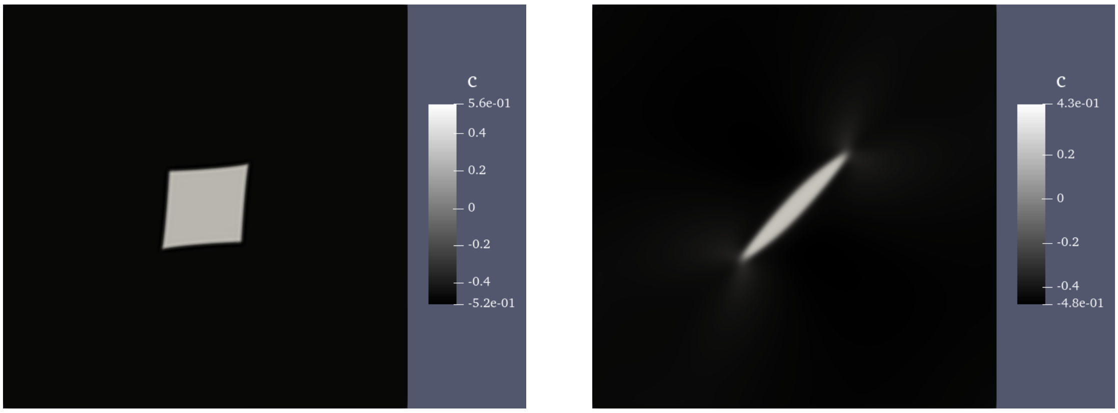

(a) **(b)**

Figure 5.16. *Simulation of the misfit strain effect on a square-shaped precipitate.* (**a**) *Initial evolution after one time step.* (**b**) *Needle-shaped precipitate at* $t = 2\,\mathrm{h}$

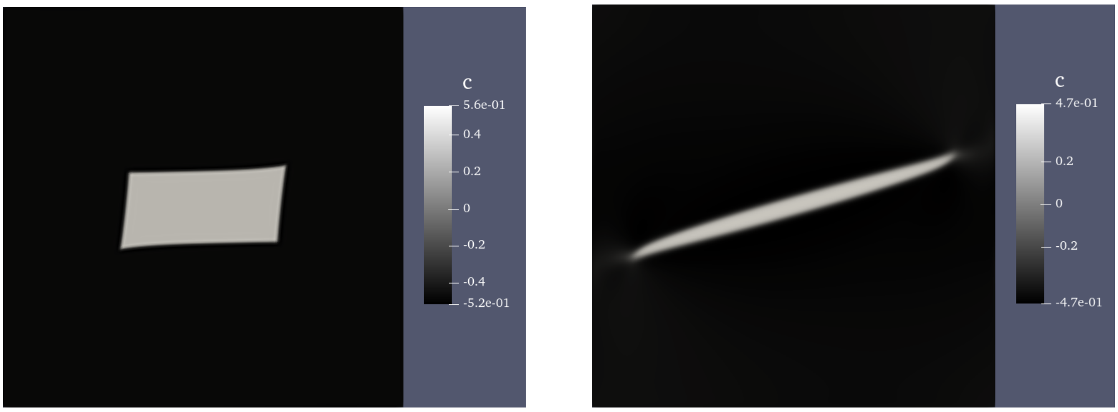

(a) **(b)**

Figure 5.17. *Simulation of the misfit strain effect on a rectangular-shaped precipitate.* (**a**) *Initial evolution after one time step.* (**b**) *Needle-shaped precipitate at* $t = 6\,\mathrm{h}$

as shown in Fig. 2.2. We may note that the needle-shaped precipitate in our simulation is less sharp than those found in real alloys, which can be explained by the use of the diffuse-interface approach in the phase-field model. We notice the same evolution for the rectangular-shaped initial precipitate in Fig. 3.5b, as shown in Fig. 5.17.

The evolution of the system containing multiple smaller initial square precipitates in Fig. 3.5c behaved differently from the previous strain field simulations, as can be seen in Fig. 5.18. At the beginning of the evolution, the square-shaped precipitates restructured themselves into needles, but then they dissolved into the matrix, leaving a single-phase system. In this case, the increase in free energy from the elastic strain energy and the interfacial energy became larger than the decrease in volumetric bulk energy due to the formation of the precipitate phase. Considering that the system evolves by minimising the total free energy of the system, it became energetically favourable for the system to dissolve the precipitates into the matrix, leaving a single-phase system. Meanwhile, for the previous simulations with elastic strain effects, the sizes of the precipitates were large enough to make the decrease in volumetric bulk energy exceed the increase due to strain and interface energy, making the needle-shaped precipitates stable in the system. This indicates the existence of a critical nucleus size needed to form a stable pre-

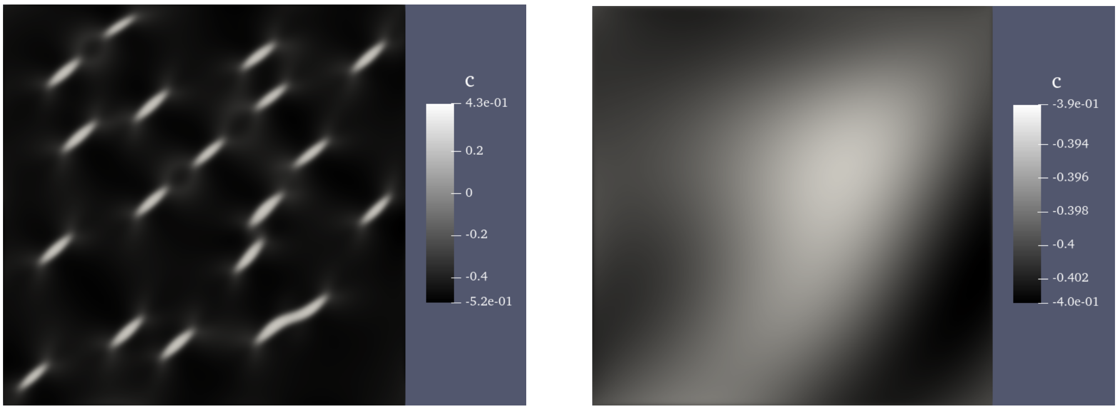

(a) **(b)**

Figure 5.18. *Simulation of the misfit strain effect on multiple square-shaped precipitates of dimensions* $6 \times 6\,\mathrm{nm}^2$. (**a**) *Needle-shaped precipitates at* $t = 120\,\mathrm{s}$. (**b**) *Precipitates dissolved into the* Al *matrix.*

cipitate. The total free energy of a critical nucleus is used in classical nucleation theory to determine the rate of nucleation, and it could therefore be of interest to calculate the critical nucleus size in future work. This would give the possibility of calculating the probability of forming a nucleation site in the microstructure, making the model better suited for studying the precipitation mechanisms in the microstructure.

We also attempted to simulate a 3-dimensional system, but in addition to a significant increase in the computational cost, it also led to problems with not having enough computer memory. The reason for this is that the Jacobian of the system becomes too large to store in the computer memory.

Chapter 6

Conclusion

The objective of this master's thesis was to study the precipitation of β'' precipitates during an artificial ageing process of 6xxx-series aluminium alloys at 450 K through computer simulations. The motivation for studying the microstructure evolution of these alloys during ageing was because this process is applied in the production of aluminium alloys in order to enhance their material properties, and for this reason it is of interest to achieve better insight into the precipitation mechanisms of the microstructure. These simulations were based upon a phase-field model that evolves the microstructure towards thermodynamic equilibrium by minimising the free energy of the system. The model was defined by applying the Cahn-Hilliard equation onto a conserved order parameter, where this order parameter denoted the composition of β'' precipitates in the system. The Cahn-Hilliard equation is a diffusion equation that models phase boundaries using a diffuse-interface approach, which is beneficial for modelling a two-phase system, as there is no need to track the interfaces like for sharp-interface models.

We looked at the effect of temperature fluctuations in the microstructure, since the formation of precipitates is expected to release heat into the system. However, assuming that the average temperature of the alloy sample is constant during the ageing process, we found that it was unnecessary to account for temperature fluctuations in the microstructure. Due to the high thermal diffusivity of aluminium alloys (like for most other metals), we calculated that the characteristic time scale for the propagation of a temperature front over a distance of 100 nm is 156 ps, which is several orders of magnitude smaller than the time step in our simulations.

We also attempted to model how applying a DC electric field across the alloy sample during the artificial ageing process affects the formation of precipitates. This process has been studied in previous experimental studies, where they noticed increased material property values and shorter ageing time before reaching peak ageing. It is therefore interesting for both scientific and commercial purposes to investigate how this field influences the precipitation process. In this work, we studied the effect of the electron wind force on the microstructure evolution, which was implemented into the phase-field model by adding an additional free energy term for the electric energy into our free energy expression and by solving a Laplace equation for the electric potential in the system. Some of the explanations that have been presented in experimental studies of the effects associated with applying an electric field have been that the field leads to more homogeneous nucleation and that the electric field increases the diffusion rate of solute atoms.

However, we did not obtain these evolution mechanisms for the precipitation in our simulations, as all of the precipitates in our simulations diffused towards one side of the system. This led us to believe that the effect of the electron wind on the semi-coherent precipitates in Al−Mg−Si alloys is small compared to the other mechanisms in the microstructure. We also discussed the fundamental difference between our phase-field model and real alloys, where the phase-field method models the precipitate phases as mobile, while β'' precipitates are considered to be immobile structures in the microstructure of real alloys.

Before we added elastic strain contributions from the misfit strain between the Al matrix and the β'' precipitates, the stable shape of the precipitates in our simulations was a circular shape. When we implemented the strain field into the simulations, we studied the evolution of initial square- and rectangular-shaped precipitates. These precipitates evolved into needle-shaped structures, which are similar to the shapes of β'' precipitates in the microstructure of real aluminium alloys. The simulations also showed that the size of the precipitates is important for their stability in the microstructure. This is related to classical nucleation theory, which states that as the size of the precipitates increase, their surface energy is compensated by change in volumetric formation energy. From this surface-to-volume ratio, a critical nucleus size marks the point where nucleation occurs spontaneously and precipitates become stable in the microstructure. Our simulations showed that the needle-shaped precipitates that evolved from initial square precipitates of dimensions $6 \times 6\,\mathrm{nm}^2$ dissolved into the matrix, indicating that these nuclei were sub-critical. Meanwhile, the needle-shaped precipitates that evolved from a square- and a rectangular-shaped precipitate of dimensions $20 \times 20\,\mathrm{nm}^2$ and $40 \times 20\,\mathrm{nm}^2$, respectively, became stable needles in the system.

Chapter 7

Future work

Some suggestions for logical ways to continue the work that has been performed in this thesis are to:

- Model similar systems using the KKS model.
- Study the effects of other electric forces on the microstructure.
- Look further into the elastic strain effects on the precipitates.

The phase-field model that was applied in this work was based on solving the Cahn-Hilliard equation, but it could be interesting to consider the Kim Kim Suzuki (KKS) model instead. It features the non-conserved order parameter η, which is driven by the Allen-Cahn equation, but it also has the added feature of expressing the total concentration order parameter c as a function of the phase concentrations (equilibrium concentrations) c_α and c_β on the form

$$c = (1 - h(\eta))\, c_\alpha + h(\eta)\, c_\beta,$$

where $h(\eta)$ is an interpolation function. Additionally, it makes the interface thickness independent of the interfacial free energy. The phase-field module in the MOOSE framework already contains several functions and kernels for the KKS model, which makes it simple to implement into a simulation.

Our phase-field model with the addition of a DC electric field considered the contributions from the electron wind force onto the system. These simulations did not exhibit the expected precipitation mechanisms from previous experimental studies, which may indicate that other effects are more important for the evolution of the microstructure. One contribution that may be interesting to study is the interactions from electric dipoles across the precipitates onto the solute atoms in the matrix, as these interactions might lead to a higher diffusion rate of solute atoms to the precipitate boundaries. By looking strictly at the effects due to electric dipoles, this would not lead to an effective force on the precipitates from the applied electric field itself, which might therefore give evolution mechanisms that are closer to those observed in experimental studies.

We briefly looked at the effects of elastic strain on the precipitates, but there are several interesting properties to investigate further connected to these effects, such as the aspect ratio of the needles and the critical nucleus size for the needles to makes them stable in the system. This could also be used to calculate the rate of nucleation using classical nucleation theory. It may be beneficial to use the KKS model for these simulations, due to the independence between the interface thickness and the interfacial free energy. This would also give the opportunity to model the strain contributions so that the precipitates can have three different spatial orientations by connecting the elastic strain to three non-conserved order parameters η_i $(i = 1, 2, 3)$.

Bibliography

[1] J. Davis, 'Aluminum and Aluminum Alloys', in *Alloying: understanding the basics*, Materials Park, OH: ASM International, 2001, pp. 315–416, ISBN: 978-0-87170-744-4.

[2] J. Hirsch, 'Aluminium in Innovative Light-Weight Car Design', *Mater. Trans.*, vol. 52, no. 5, pp. 818–824, 2011. DOI: 10.2320/matertrans.L-MZ201132.

[3] T. Dursun and C. Soutis, 'Recent developments in advanced aircraft aluminium alloys', *Materials & Design (1980-2015)*, vol. 56, pp. 862–871, Apr. 2014. DOI: 10.1016/j.matdes.2013.12.002.

[4] J. Banhart, C. S. T. Chang, Z. Liang, N. Wanderka, M. D. H. Lay and A. J. Hill, 'Natural Aging in Al-Mg-Si Alloys - A Process of Unexpected Complexity', *Adv. Eng. Mater.*, vol. 12, no. 7, pp. 559–571, Jul. 2010. DOI: 10.1002/adem.201000041.

[5] 'Heat Treating of Aluminum Alloys', in *ASM handbook. 4: Heat treating*, ASM International, 1991, pp. 841–879, ISBN: 978-0-87170-379-8.

[6] P. Wang *et al.*, 'A review of particulate-reinforced aluminum matrix composites fabricated by selective laser melting', *Transactions of Nonferrous Metals Society of China*, vol. 30, no. 8, pp. 2001–2034, Aug. 2020. DOI: 10.1016/S1003-6326(20)65357-2.

[7] L. He, Q. Ning, M. Wei, X. Wang and J. Cui, 'Investigation of precipitation and tensile properties of 7B04 under direct current and aging', *Materials Science and Engineering: A*, vol. 801, p. 140 112, Jan. 2021. DOI: 10.1016/j.msea.2020.140112.

[8] Y. Onodera and K.-I. Hirano, ‘The effect of direct electric current on precipitation in a bulk Al-4 wt % Cu alloy’, *J Mater Sci*, vol. 11, no. 5, pp. 809–816, May 1976. DOI: 10.1007/BF00542295.

[9] J. Zhang, L. Zhan and S. Jia, ‘Effects of Electric Pulse Current on the Aging Kinetics of 2219 Aluminum Alloy’, *Advances in Materials Science and Engineering*, vol. 2014, pp. 1–8, 2014. DOI: 10.1155/2014/240879.

[10] K. Jung and H. Conrad, ‘External electric field applied during solution heat treatment of the Al-Mg-Si alloy AA6022’, *Journal of Materials Science*, vol. 39, no. 21, pp. 6483–6486, Nov. 2004. DOI: 10.1023/B:JMSC.0000044886.66798.95.

[11] C. Marioara, S. Andersen, J. Jansen and H. Zandbergen, ‘Atomic model for GP-zones in a 6082 Al–Mg–Si system’, *Acta Materialia*, vol. 49, no. 2, pp. 321–328, Jan. 2001. DOI: 10.1016/S1359-6454(00)00302-5.

[12] N. Moelans, B. Blanpain and P. Wollants, ‘An introduction to phase-field modeling of microstructure evolution’, *Calphad*, vol. 32, no. 2, pp. 268–294, Jun. 2008. DOI: 10.1016/j.calphad.2007.11.003.

[13] D. Li and L. Chen, ‘Computer simulation of stress-oriented nucleation and growth of ϑ’ precipitates in Al–Cu alloys’, *Acta Materialia*, vol. 46, no. 8, pp. 2573–2585, May 1998. DOI: 10.1016/S1359-6454(97)00478-3.

[14] D. Kleiven and J. Akola, ‘Precipitate formation in aluminium alloys: Multiscale modelling approach’, *Acta Materialia*, vol. 195, pp. 123–131, Aug. 2020. DOI: 10.1016/j.actamat.2020.05.050.

[15] L.-Q. Chen, ‘Phase-Field Models for Microstructure Evolution’, *Annual Review of Materials Research*, vol. 32, no. 1, pp. 113–140, 2002. DOI: 10.1146/annurev.matsci.32.112001.132041.

[16] C. J. Permann *et al.*, ‘MOOSE: Enabling massively parallel multiphysics simulation’, *SoftwareX*, vol. 11, p. 100 430, Jan. 2020. DOI: 10.1016/j.softx.2020.100430.

[17] *6106 (6106-T6, AlMgSiMn) Aluminum :: MakeItFrom.com.* [Online]. Available: https://www.makeitfrom.com/material-properties/6106-6106-T6-AlMgSiMn-Aluminum (visited on 5th Apr. 2022).

[18] G. Mrówka-Nowotnik, 'Influence of chemical composition variation and heat treatment on microstructure and mechanical properties of 6xxx alloys', *Archives of Materials Science and Engineering*, vol. 46, no. 2, pp. 98–107, 2010.

[19] S. J. Andersen, C. D. Marioara, J. Friis, S. Wenner and R. Holmestad, 'Precipitates in aluminium alloys', *Advances in Physics: X*, vol. 3, no. 1, p. 1 479 984, Jan. 2018. DOI: 10.1080/23746149.2018.1479984.

[20] C. D. Marioara, S. J. Andersen, H. W. Zandbergen and R. Holmestad, 'The influence of alloy composition on precipitates of the Al-Mg-Si system', *Metallurgical and Materials Transactions A*, vol. 36, no. 3, pp. 691–702, Mar. 2005. DOI: 10.1007/s11661-005-0185-1.

[21] R. Lumley, Ed., *Fundamentals of aluminium metallurgy: production, processing and applications*, ser. Woodhead publishing in materials. Oxford: Woodhead Publ, 2011, ISBN: 978-1-84569-654-2.

[22] K. Matsuda *et al.*, 'Precipitation sequence of various kinds of metastable phases in Al-1.0mass% Mg2Si-0.4mass% Si alloy', *Journal of Materials Science*, vol. 35, no. 1, pp. 179–189, 2000. DOI: 10.1023/A:1004769305736.

[23] S. Andersen, H. Zandbergen, J. Jansen, C. Træholt, U. Tundal and O. Reiso, 'The crystal structure of the β" phase in Al–Mg–Si alloys', *Acta Materialia*, vol. 46, no. 9, pp. 3283–3298, May 1998. DOI: 10.1016/S1359-6454(97)00493-X.

[24] Ø. T. Nygård, 'Kinetic Monte Carlo simulations of the early stages of precipitation in Al-Mg-Si alloys using ab initio based activation energies', M.S. thesis, Norwegian University of Science and Technology, 2020. [Online]. Available: https://hdl.handle.net/11250/2785541.

[25] P. H. Ninive *et al.*, ‘Detailed atomistic insight into the β” phase in Al–Mg–Si alloys’, *Acta Materialia*, vol. 69, pp. 126–134, 2014. DOI: https://doi.org/10.1016/j.actamat.2014.01.052.

[26] Y. Deyan, Z. Mingzhe, Q. Ning, C. Zhiquan and Y. Danqing, ‘Precipitation Behavior of Al-Cu-Mg Alloy During Electric Field-Assisted Aging’, *Journal of Materials Engineering and Performance*, vol. 22, no. 1, pp. 206–209, Jan. 2013. DOI: 10.1007/s11665-012-0212-5.

[27] J. W. Cahn and J. E. Hilliard, ‘Free Energy of a Nonuniform System. I. Interfacial Free Energy’, *The Journal of Chemical Physics*, vol. 28, no. 2, pp. 258–267, Feb. 1958. DOI: 10.1063/1.1744102.

[28] J. W. Cahn and S. M. Allen, ‘A microscopic theory for domain wall motion and its experimental verification in Fe-Al alloy domain growth kinetics’, *Le Journal de Physique Colloques*, vol. 38, no. C7, pp. C7–51–C7–54, Dec. 1977. DOI: 10.1051/jphyscol:1977709.

[29] R. G. Parr and W. Yang, *Density-functional theory of atoms and molecules*, ser. International series of monographs on chemistry 16. New York : Oxford [England]: Oxford University Press ; Clarendon Press, 1989, ISBN: 978-0-19-504279-5.

[30] K. Binder, ‘Theory of first-order phase transitions’, *Reports on Progress in Physics*, vol. 50, no. 7, pp. 783–859, Jul. 1987. DOI: 10.1088/0034-4885/50/7/001.

[31] J. V. Alemán *et al.*, ‘Definitions of terms relating to the structure and processing of sols, gels, networks, and inorganic-organic hybrid materials (IUPAC Recommendations 2007)’, *Pure and Applied Chemistry*, vol. 79, no. 10, pp. 1801–1829, Jan. 2007. DOI: 10.1351/pac200779101801.

[32] D. W. Malone and R. E. Hummel, ‘Electromigration in integrated circuits’, *Critical Reviews in Solid State and Materials Sciences*, vol. 22, no. 3, pp. 199–238, Sep. 1997. DOI: 10.1080/10408439708241261.

[33] W. Wang, Z. Suo and T.-H. Hao, 'A simulation of electromigration-induced transgranular slits', *Journal of Applied Physics*, vol. 79, no. 5, pp. 2394–2403, Mar. 1996. DOI: 10.1063/1.361166.

[34] S.-B. Liang, C.-B. Ke, M.-Y. Tan, M.-B. Zhou and X.-P. Zhang, 'Phase field simulation of the microstructural evolution and electromigration-induced phase segregation in line-type Cu/Sn-Bi/Cu solder interconnects', in *2016 17th International Conference on Electronic Packaging Technology (ICEPT)*, Wuhan, China: IEEE, Aug. 2016, pp. 836–840. DOI: 10.1109/ICEPT.2016.7583260.

[35] A. G. Khachaturyan, S. Semenovskaya and T. Tsakalakos, 'Elastic strain energy of inhomogeneous solids', *Phys. Rev. B*, vol. 52, no. 22, pp. 15 909–15 919, Dec. 1995. DOI: 10.1103/PhysRevB.52.15909.

[36] L. K. Aagesen, D. Schwen, K. Ahmed and M. R. Tonks, 'Quantifying elastic energy effects on interfacial energy in the Kim-Kim-Suzuki phase-field model with different interpolation schemes', *Computational Materials Science*, vol. 140, pp. 10–21, Dec. 2017. DOI: 10.1016/j.commatsci.2017.08.005.

[37] S. DeWitt *et al.*, 'Misfit-driven β"' precipitate composition and morphology in Mg-Nd alloys', *Acta Materialia*, vol. 136, pp. 378–389, Sep. 2017. DOI: 10.1016/j.actamat.2017.06.053.

[38] B. Bhadak, R. Sankarasubramanian and A. Choudhury, 'Phase-Field Modeling of Equilibrium Precipitate Shapes Under the Influence of Coherency Stresses', *Metallurgical and Materials Transactions A*, vol. 49, no. 11, pp. 5705–5726, Nov. 2018. DOI: 10.1007/s11661-018-4835-5.

[39] A. R. Natarajan, E. L. Solomon, B. Puchala, E. A. Marquis and A. Van der Ven, 'On the early stages of precipitation in dilute Mg–Nd alloys', *Acta Materialia*, vol. 108, pp. 367–379, Apr. 2016. DOI: 10.1016/j.actamat.2016.01.055.

[40] *Specific Heat of common Substances*, 2003. [Online]. Available: https://www.engineeringtoolbox.com/specific-heat-capacity-d_391.html (visited on 5th Apr. 2022).

[41] *Thermal Diffusivity Table*. [Online]. Available: https://www.engineersedge.com/heat_transfer/thermal_diffusivity_table_13953.htm (visited on 10th Jan. 2021).

[42] A. Jokisaari, W. Wu, P. Voorhees, J. Guyer, J. Warren and O. Heinonen, 'Phase field benchmark problems targeting fluid flow and electrochemistry', *Computational Materials Science*, vol. 176, p. 109 548, Apr. 2020. DOI: 10.1016/j.commatsci.2020.109548.

[43] J. Burke and T. R. Ramachandran, 'Self-diffusion in aluminum at low temperatures', *Metallurgical and Materials Transactions B*, vol. 3, no. 1, pp. 147–155, Jan. 1972. DOI: 10.1007/BF02680593.

[44] W. Research, *ElementData*, 2014. [Online]. Available: https://reference.wolfram.com/language/ref/ElementData.html (visited on 10th Apr. 2022).

[45] A. Jain *et al.*, 'Commentary: The Materials Project: A materials genome approach to accelerating materials innovation', *APL Materials*, vol. 1, no. 1, p. 011 002, Jul. 2013. DOI: 10.1063/1.4812323.

[46] M. de Jong *et al.*, 'Charting the complete elastic properties of inorganic crystalline compounds', *Sci Data*, vol. 2, no. 1, p. 150 009, Dec. 2015. DOI: 10.1038/sdata.2015.9.

[47] ScienceDirect, *Stiffness Tensor*. [Online]. Available: https://www.sciencedirect.com/topics/engineering/stiffness-tensor (visited on 11th Apr. 2022).

[48] *Materials Data on Al by Materials Project*, Type: dataset, 2020. DOI: 10.17188/1189564. [Online]. Available: https://www.osti.gov/servlets/purl/1189564/.

[49] *Materials Data on Mg5Si6 by Materials Project*, Type: dataset, 2020. DOI: 10.17188/1274352. [Online]. Available: https://www.osti.gov/servlets/purl/1274352/.

[50] J. Frafjord, S. Dumoulin, S. Wenner, I. G. Ringdalen, R. Holmestad and J. Friis, 'Fully resolved strain field of the β" precipitate calculated by density functional theory', *Computational Materials Science*, vol. 187, p. 110 054, Feb. 2021. DOI: 10.1016/j.commatsci.2020.110054.

[51] M. R. Tonks, D. Gaston, P. C. Millett, D. Andrs and P. Talbot, 'An object-oriented finite element framework for multiphysics phase field simulations', *Computational Materials Science*, vol. 51, no. 1, pp. 20–29, Jan. 2012. DOI: 10.1016/j.commatsci.2011.07.028.

[52] T. S. Trogden, 'Introduction to phase field modelling', B.Sc. Brigham Young University, Idaho, Apr. 2019.

[53] R. P. Sear, 'Nucleation: Theory and applications to protein solutions and colloidal suspensions', *Journal of Physics: Condensed Matter*, vol. 19, no. 3, p. 033 101, Jan. 2007. DOI: 10.1088/0953-8984/19/3/033101.

[54] G. S. Gupta, S. Sarkar, A. Chychko, L. Teng, M. Nzotta and S. Seetharaman, 'Process Concept for Scaling-Up and Plant Studies', in *Treatise on Process Metallurgy*, Elsevier, 2014, pp. 1100–1144, ISBN: 978-0-08-096988-6. DOI: 10.1016/B978-0-08-096988-6.00040-7.

Appendix

A Input file for phase-field simulation with strain contributions in MOOSE

The following example input file simulates the temporal evolution of an initial rectangular-shaped precipitate using the phase-field model with elastic strain contributions from misfit strain.

```
[Mesh]
  # Generate a 2D, 100nm x 100nm mesh
  type = GeneratedMesh
  dim = 2
  nx = 100
  ny = 100
  xmin = 0
  xmax = 100
  ymin = 0
  ymax = 100
  uniform_refine = 1
[]

[Variables]
  [c] # Composition of Mg5Si6 (unitless) from -1 to 1
    order = FIRST
    family = LAGRANGE
  []
  [w] # Chemical potential
    order = FIRST
    family = LAGRANGE
  []
  [disp_x]
    order = FIRST
    family = LAGRANGE
```

```
  []
  [disp_y]
    order = FIRST
    family = LAGRANGE
  []
[]

[AuxVariables]
  [f_density] # Local energy density (keV/nm^3)
    order = CONSTANT
    family = MONOMIAL
  []
[]

[GlobalParams]
  block = 0
  displacements = 'disp_x disp_y'
[]

[ICs]
  [concentrationIC] # Rectangular-shaped initial precipitate
    type = MultiBoundingBoxIC
    corners =           '30 40 0'
    opposite_corners =  '70 60 0'
    inside = '0.4734'
    outside = '-0.4734'
    variable = c
  []
[]

[BCs]
  # Periodic boundaries are usually applied in phase-field models
  [Periodic]
    # Periodic concentration and chem. pot
    [c_w_bcs]
      variable = 'c w'
      auto_direction = 'x y'
    []
  []
  # Dirichlet boundaries for displacements on left/right
  [left_disp_x]
    type = DirichletBC
    variable = 'disp_x'
```

```
    boundary = 'left'
    value = 0
  []
  [right_disp_x]
    type = DirichletBC
    variable = 'disp_x'
    boundary = 'right'
    value = 0
  []
  [left_disp_y]
    type = DirichletBC
    variable = 'disp_y'
    boundary = 'left'
    value = 0
  []
  [right_disp_y]
    type = DirichletBC
    variable = 'disp_y'
    boundary = 'right'
    value = 0
  []
  # Dirichlet boundaries for displacements on top/bottom
  [top_disp_x]
    type = DirichletBC
    variable = 'disp_x'
    boundary = 'top'
    value = 0
  []
  [bottom_disp_x]
    type = DirichletBC
    variable = 'disp_x'
    boundary = 'bottom'
    value = 0
  []
  [top_disp_y]
    type = DirichletBC
    variable = 'disp_y'
    boundary = 'top'
    value = 0
  []
  [bottom_disp_y]
    type = DirichletBC
    variable = 'disp_y'
```

```
    boundary = 'bottom'
    value = 0
  []
[]

[Kernels]
  # Cahn-Hilliard equation
  [c_dot]
    type = CoupledTimeDerivative
    variable = w
    v = c
  []
  [coupled_res]
    type = SplitCHWRes
    variable = w
    mob_name = M
  []
  [coupled_parsed]
    type = SplitCHParsed
    variable = c
    f_name = f_loc
    kappa_name = kappa_c
    w = w
  []
  # Mechanical equilibrium equation
  [TensorMechanics]
  []
[]

[AuxKernels]
  [f_density] # Calculates the energy density by combining the
              # local, gradient and strain energy (keV/nm^3)
    type = TotalFreeEnergy
    variable = f_density
    f_name = 'f_loc'
    kappa_names = 'kappa_c'
    interfacial_vars = c
  []
[]

[Materials]
  [constants]
    type = GenericFunctionMaterial
```

```
    prop_names = 'kappa_c T'
    prop_values = '0.0018973 450'
  []
  [mobility] # nm^5/keV s
    type = DerivativeParsedMaterial
    f_name = 'M'
    args = 'c'
    constant_names = 'M_0' # D*V_m/RT, V_m=1e22 nm^3
    constant_expressions = '34.04'
    function = 'M_0*(1+c)*(1-c)/4'
    derivative_order = 1
  []
  [elasticity_tensor_al] # keV/nm^3
    type = ComputeElasticityTensor
    base_name = 'C_al'
    C_ijkl = '104 73 73 104 73 104 32 32 32' # GPa
    fill_method = symmetric9
    # giga * J->eV / kilo / m^3->nm^3
    elasticity_tensor_prefactor = '6.241809e-3'
  []
  [elasticity_tensor_mg5si6] # keV/nm^3
    type = ComputeElasticityTensor
    base_name = 'C_mg5si6'
    C_ijkl = '101 51 50 0 -8 0 80 55 0 3 0 76 0 10 0 16 0 1 32 0
     ↪  29' # GPa
    fill_method = symmetric21
    # giga * J->eV / kilo / m^3->nm^3
    elasticity_tensor_prefactor = '6.241809e-3'
  []
  [w_al]
    type = DerivativeParsedMaterial
    f_name = 'w_al'
    args = 'c'
    function = (0.4734-c)/(2*0.4734)
  []
  [w_mg5si6]
    type = DerivativeParsedMaterial
    f_name = 'w_mg5si6'
    args = 'c'
    function = (c+0.4734)/(2*0.4734)
  []
  [C]
    type = CompositeElasticityTensor
```

```
    args = 'c'
    tensors = 'C_mg5si6 C_al'
    weights = 'w_mg5si6 w_al'
  []
  [strain]
    type = ComputeSmallStrain
    eigenstrain_names = 'misfit_strain'
  []
  [stress]
    type = ComputeLinearElasticStress
  []
  [misfit_dep]
    type = DerivativeParsedMaterial
    f_name = 'misfit_dep'
    args = 'c'
    function = (c+0.4734)/(2*0.4734)
    enable_jit = true
  []
  [misfit]
    type = ComputeVariableEigenstrain
    eigen_base = '-0.06718336 -0.12987458 -0.00590827 0 0
     ↪  0.15421595'
    args = 'c'
    prefactor = misfit_dep
    eigenstrain_name = misfit_strain
  []
  [local_energy]
    type = DerivativeParsedMaterial
    f_name = 'f_c'
    args = 'c'
    constant_names = 'T_c T_ref c_ref B'    #[c_ref] = eV/nm^3 K
    constant_expressions = '580 298 0.01510 c_ref*T_c^2/(2*T_ref)'
    function = '1e-3*B*(2*(T-T_c)*c^2/T_c + c^4)' # keV/nm^3
    material_property_names = 'T'
    derivative_order = 2
  []
  [elastic_energy]
    type = ElasticEnergyMaterial
    f_name = 'f_elastic'
    args = 'c'
  []
  [free_energy]
    type = DerivativeSumMaterial
```

```
    f_name = 'f_loc'
    sum_materials = 'f_c f_elastic' # keV/nm^3
    args = 'c'
    derivative_order = 2
    outputs = exodus
  []
  [precipitate_indicator]
    type = ParsedMaterial
    f_name = 'prec_indic'
    args = 'c'
    constant_names = 'T_c'
    constant_expressions = '580'
    material_property_names = 'T'
    function = if(c>((T_c-T)/T_c)^(0.5)-0.1,0.0001,0)
    outputs = exodus
  []
[]

[Postprocessors]
  [evaluations]
    type = NumResidualEvaluations
  []
  [step_size]
    type = TimestepSize
  []
  [iterations]
    type = NumNonlinearIterations
  []
  [nodes]
    type = NumNodes
  []
  [active_time]
    type = PerfGraphData
    section_name = 'Root'
    data_type = total
  []
  [precipitate_area]
    type = ElementIntegralMaterialProperty
    mat_prop = prec_indic
  []
  [total_energy]
    type = ElementIntegralVariablePostprocessor
    variable = f_density
```

```
  []
[]

[Preconditioning]
  [coupled]
    type = SMP
    full = true
  []
[]

[Executioner]
  type = Transient
  scheme = bdf2
  solve_type = PJFNK
  petsc_options_iname = '-pc_type -sub_pc_type'
  petsc_options_value = 'asm lu'
  l_max_its = 30
  l_tol = 1e-5
  nl_max_its = 30
  nl_abs_tol = 1e-7
  end_time = 21600 # 6 hours
  automatic_scaling = true
  [TimeStepper]
    type = SolutionTimeAdaptiveDT
    dt = 0.1
  []
[]

[Debug]
  show_var_residual_norms = true
[]

[Outputs]
  exodus = true
  console = true
  csv = true
  sync_times = '1800 3600 5400'
  perf_graph = true
  [console]
    type = Console
    max_rows = 10
  []
  [other]
```

```
    type = Exodus
    interval = 10
  []
[]
```

NTNU

Norwegian University of
Science and Technology